Earth and Planetary Science Letters 458 (2017) 92–106

Contents lists available at ScienceDirect

Earth and Planetary Science Letters

www.elsevier.com/locate/epsl

Neoproterozoic paleogeography of the Tarim Block: An extended or alternative "missing-link" model for Rodinia?

Bin Wen [a,b], David A.D. Evans [b], Yong-Xiang Li [a,*]

[a] State Key Laboratory for Mineral Deposits Research, School of Earth Sciences and Engineering, Institute of Geophysics and Geodynamics, Nanjing University, Nanjing 210046, China
[b] Department of Geology and Geophysics, Yale University, New Haven, CT 06520-8109, USA

ARTICLE INFO

Article history:
Received 27 June 2016
Received in revised form 14 October 2016
Accepted 16 October 2016
Available online 9 November 2016
Editor: A. Yin

Keywords:
Tarim Block
paleomagnetism
Neoproterozoic
missing-link
Rodinia
supercontinent

ABSTRACT

Recent reconstructions of the Rodinia supercontinent and its breakup incorporate South China as a "missing link" between Australia and Laurentia, and place the Tarim craton adjacent to northwestern Australia on the supercontinent's periphery. However, subsequent kinematic evolution toward Gondwana amalgamation requires complex geometric shuffling between South China and Tarim, which cannot be easily resolved with the stratigraphic records of those blocks. Here we present new paleomagnetic data from early Ediacaran strata of northwest Tarim, and document large-scale rotation at near-constant paleolatitudes during Cryogenian time. The rotation is coeval with Rodinia breakup, and Tarim's paleolatitudes are compatible with its placement between Australia and Laurentia, either by itself as an alternative "missing link" or joined with South China in that role. At the same time, indications of subduction-related magmatism in Tarim's Neoproterozoic record suggest that Rodinia breakup was dynamically linked to subduction retreat along its northern margin. Such a model is akin to early stages of Jurassic fragmentation within southern Gondwana, and implies more complicated subduction-related dynamics of supercontinent breakup than superplume impingement alone.

1. Introduction

The evolution of the Neoproterozoic supercontinent Rodinia was an integral part of the broader Earth system that also included extremes in paleoclimate (Kirschvink, 1992), ocean geochemistry (Halverson et al., 2010), and the emergence of complex life (McMenamin and McMenamin, 1990). However, much debate remains regarding the configuration of this supercontinent (e.g., Li et al., 2008; Evans, 2013). One main controversy is whether Australia–East Antarctica was directly connected to Laurentia, near the center of Rodinia (Hoffman, 1991; Li et al., 2008), and if so, in what specific configuration. Early Rodinia models postulated a tight fit of those cratons, establishing the standard "SWEAT" (Southwest U.S.–East Antarctic) connection (e.g., Dalziel, 1997). Simultaneously or shortly afterwards, alternative models were proposed, including the "AUSWUS" (Australia–Western United States) connection (Karlstrom et al., 1999), the "AUSMEX" (Australia–Mexico) juxtaposition (Wingate et al., 2002), and also the "Missing-link" model of South China inserted in between (Li et al., 1995). According to a comprehensive analysis of geological and paleomagnetic data (summarized by Li et al., 2008), only the "Missing-link" model was demonstrated to be viable by both geological correlations and ca. 1200–750 Ma paleomagnetic poles from Australia and Laurentia. For example, the ca. 750 Ma paleomagnetic data demanded either untenably early supercontinental breakup relative to the stratigraphic age of proposed rift–drift transitions on the Australian and Laurentian conjugate margins, or a sizable gap between the blocks (Wingate and Giddings, 2000). South China may have filled that gap, as its centrally located, Grenville-age Sibao (or Jiangnan) orogen could mark the suture between the Australia–proximal Yangtze block and the Laurentia-related Cathaysia block during Rodinia amalgamation (Li et al., 1995, 2008).

However, the basis for this "missing-link" position for South China faces some challenges. First, the timing of the assembly of Yangtze and Cathaysia, i.e., the age of the Sibao or Jiangnan orogen is probably younger than the type Grenville orogeny suggested by new chronologic data (e.g., Zhao et al., 2011; Wang et al., 2014), and the tectonic setting of the younger magmatism (ca. 830–750 Ma) in this block has different interpretations (e.g., Sun et al., 2008). Second, in order for South China to migrate from the "missing link" position to a likely early Paleozoic location adjacent to NW Australia, South China must have taken a circuitous path around northern Australia (Li et al., 2013)—

* Corresponding author.
E-mail address: yxli@nju.edu.cn (Y.-X. Li).

http://dx.doi.org/10.1016/j.epsl.2016.10.030
0012-821X/

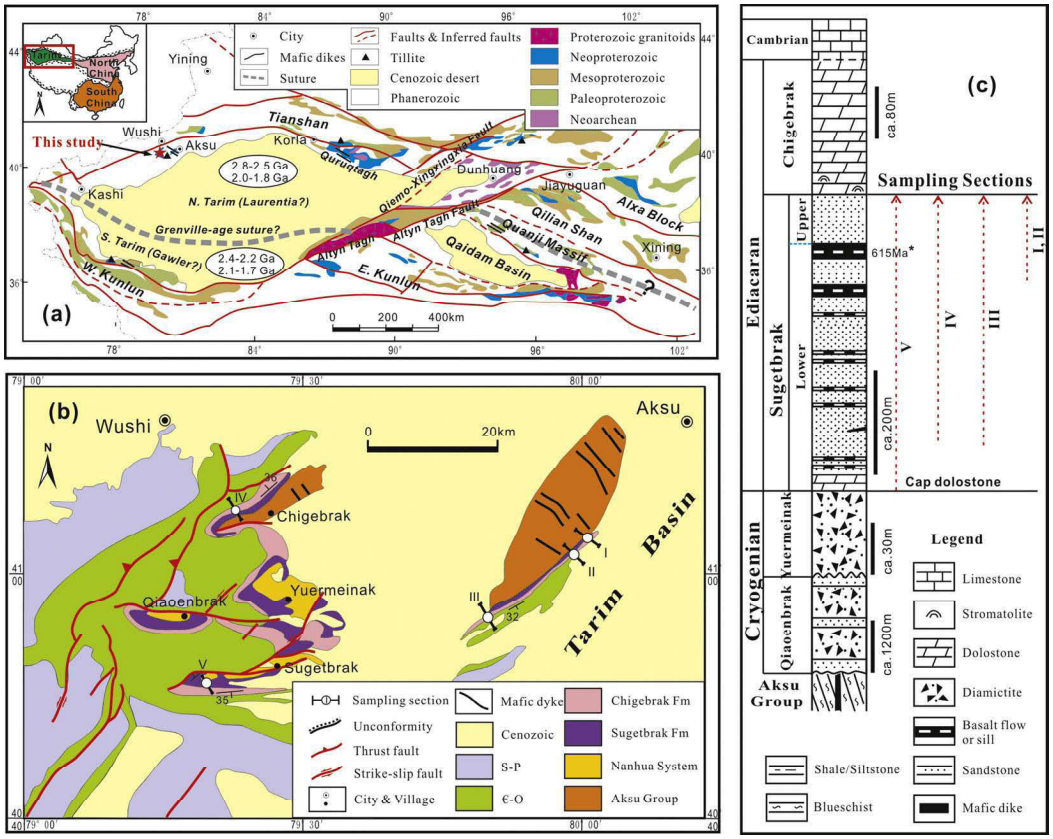

Fig. 1. (a) Tectonic framework of Tarim Block (NW China), showing the Grenville-age "Tarimian" sutures (after Lu et al., 2008; Z.Q. Xu et al., 2013) and study area in this work. The ovals mark the different age ranges of continental nucleus and igneous/metamorphic events in basements of Northern and Southern Tarim. (b) Geological map of the northwestern margin of Tarim Block (after Gao et al., 1985; XBGMR, 1993; Turner, 2010; Wen et al., 2015), showing the sampling sections. (c) The composite Precambrian stratigraphic column of the Aksu–Wushi area (after Gao et al., 1985; XBGMR, 1993; Turner, 2010; Zhu et al., 2011; B. Xu et al., 2013; Wen et al., 2015), schematically showing the sampling sections I to V that consist of the upper and lower part of the Sugetbrak Formation. Cross-section of each section is shown in Fig. S1. *, a U–Pb zircon age of basalt from B. Xu et al. (2013). Note variable thickness scales.

not only is this kinematically unusual, but it also predicts large-scale sinistral transform motion that is not readily compatible with the Ediacaran–Cambrian passive-margin tectonostratigraphic records of both blocks (e.g., Jiang et al., 2003). As an alternative to the "missing-link" position, South China has been proposed to remain near NW Australia at marginal regions of Rodinia during the evolution from Rodinia to Gondwana (Jiang et al., 2003; Zhang et al., 2013).

While South China has been placed on either side of Australia in Rodinia reconstructions, the Tarim craton has conventionally been positioned along Australia's northwestern margin at Rodinia's periphery. Such a location was initially proposed by Li et al. (1996) to account for (i) the allegedly minor role of Grenville-age tectonism in Tarim, (ii) plume-related magmatism at 830–750 Ma correlated with that in northwestern Australia, and (iii) similar Ediacaran–Cambrian stratigraphic records including late Neoproterozoic glacial deposits and Lower Cambrian volcanic rocks. Most subsequent work has adopted this model in the absence of additional constraints (e.g., Li et al., 2008); a notable exception is that of Lu et al. (2008), who instead joined Tarim with South China in the "missing link" location based on the tectonostratigraphic correlation including the ~820 Ma giant radiating dyke swarms in the center. Further work has demonstrated that the proposed location of Tarim adjacent to northwestern Australia may be ill-founded. A comprehensive study of deep-drill cores in Tarim has revealed that the Grenville-age (1.1–1.0 Ga) orogeny is in fact pervasive across the craton (Fig. 1a; Z.Q. Xu et al., 2013 and references therein). Furthermore, the 830–750 Ma magmatism in Tarim could be linked to either NW Australia, or many other locations around Australia or even other continents (Li et al., 2003, 2008). Meanwhile, the <750 Ma rifting-related magmatism that occurred in Tarim (Xu et al., 2005, 2009) is not present in northwestern Australia. And finally, the Cambrian mafic magmatism within sections of NE Tarim is found to be earliest Cambrian in age (Yao et al., 2005), and hence cannot be considered a match for the Early–Middle Cambrian Kalkarindji large igneous province in northern Australia (Glass and Phillips, 2006). Thus, the only point of distinctive geologic comparison between Tarim and northern Australia is the presence of mid–late Ediacaran glacial strata, which nonetheless lack precise age constraints and are among a handful of other enigmatic glaciogenic deposits of that age interval worldwide (Evans and Raub, 2011). Besides the geological mismatches, the other weakness for the Tarim–NW Australia juxtaposition is from the paleomagnetic constraints of Tarim. Chen et al. (2004), Zhan et al. (2007) and Zhao et al. (2014) together proposed a long connection between Tarim and NW Australia during most of the Neoproterozoic times. Not to mention its incompatibility with the geological records above, its paleolatitude is not easy to be reconciled with the paleomagnetic data obtained from the ca. 740 Ma Baiyisi volcanic rocks (Huang et al., 2005) and the Sturtian-age Qiaoenbrak Formation (Fm) sediments (Wen et al., 2013).

Apart from the oft-suggested connection to NW Australia, the other proposed paleoposition for Tarim is the eastern side of Australia (e.g., Lu et al., 2008). If so, whether the Tarim Block can act as an alternative missing link within Rodinia reconstructions? Also, the discrepancy among the available paleopoles for Tarim's paleogeography within this supercontinent emphasizes the need of more reliable paleomagnetic data. In this paper, we report high-

quality paleomagnetic data from the Ediacaran strata of northwestern Tarim (Fig. 1). Together with previously published paleomagnetic results and newly reported geological data, we present an alternative "missing-link" configuration of Rodinia by fitting the Tarim Block between Australia–East Antarctica and Laurentia, and further explore the dispersal process of this supercontinent.

2. Geological setting and sampling

The Aksu–Wushi area, bounded to the north by the Tianshan Mountains, lies along the northwestern margin of the Tarim Block (Fig. 1). The Precambrian successions preserved in this area have been well documented and are critical in understanding the tectonic evolution of this craton in the Neoproterozoic (Nakajima et al., 1990; Chen et al., 2004; Zhan et al., 2007; Wen et al., 2013; B. Xu et al., 2013; He et al., 2014). The successions comprise, from the bottom to the top, the Proterozoic schistose basement of Aksu Group and its unconformably overlying, unmetamorphosed sedimentary cover. The intensely deformed Aksu Group comprises metasedimentary rocks and mafic schists, including blue- and greenschists, which were intruded by a series of unmetamorphosed NW-trending mafic dikes (Aksu dikes; Fig. 1b). The blueschist-facies recrystallization has been interpreted to document a Proterozoic subduction–accretion complex (Nakajima et al., 1990; Zhu et al., 2011). The sedimentary cover consists of the Cryogenian Qiaoenbrak Fm and Yuermeinak Fm, and the Ediacaran Sugetbrak and Chigebrak Fms (Fig. 1b and c; Gao et al., 1985; XBGMR, 1993; Turner, 2010; Zhu et al., 2011; B. Xu et al., 2013; Wen et al., 2015). Both the Qiaoenbrak and Yuermeinak Fms are dominated by sandstone, siltstone and conglomerate, and each contains a glacial interval (Gao et al., 1985; Gao and Qian, 1985; XBGMR, 1993; Zhu and Wang, 2011; Wen et al., 2015). Recently discovered Marinoan-age cap dolostone atop the glacial deposits of Yuermeinak Fm (Fig. 1c; Wen et al., 2015), forms the base of the Ediacaran Sugetbrak Fm (400–450 m) at ca. 635 Ma by correlation (Knoll et al., 2006; Calver et al., 2013). Conformably overlying the cap carbonate is a ca. 10-m-thick red shale or siltstone unit, grading upwards into the lower red fluvial sandstone interbedded with several layers of basalt flows and an upper yellow–greenish lacustrine/shallow-marine siltstone (Fig. 1c; Turner, 2010; B. Xu et al., 2013). A recent U–Pb zircon age of ca. 615 Ma (615.2 ± 4.8 Ma and 614.4 ± 9.1 Ma; B. Xu et al., 2013) was obtained from the basalt layers within the middle Sugetbrak Fm (Fig. 1c). This age is broadly consistent with the maximum depositional age (ca. 620–602 Ma) identified by detrital zircon dating from the upper part of the formation (Zhu et al., 2011; He et al., 2014). The Chigebrak Fm conformably overlies the Sugetbrak Fm, and is mainly composed of thickly bedded stromatolitic dolostone/limestone that was interpreted by Turner (2010) to represent an extensive lake or a marine transgressive environment. The top of the Chigebrak Fm is truncated disconformably by a 5-m-thick, earliest Cambrian black chert–phosphorite layer (Gao et al., 1985; Yao et al., 2005).

We collected samples of the Ediacaran Sugetbrak Fm, including the basal cap carbonate and the overlying sandstone and basalt, from five sections (I–V) in the study area (Fig. 1b and c). Only section V contains the basal cap carbonate; the bases of the other four sections are unconformities omitting any cap carbonate that may have originally existed (cf. Fig. S1 for detailed cross-sections and sampling in the supplemental file). Cores were sampled using a portable gasoline-powered drill for most sites, and block samples were collected from sites with particularly steep access. All cores were oriented using both magnetic and solar compasses, while the orientations of block samples were measured with a magnetic compass. For block-sampled sites, declinations of magnetic variation were assigned values comparable to those calculated from nearby drilled sites. In section V (Fig. S1), a 2 m-wide mafic dike, and Sugetbrak host samples from varying distances away, were collected for a baked-contact test (AK6-16). The dike is slightly undulose in orientation, but has a general NW strike and moderate NE dip; when the moderately S-dipping (Fig. S1) host rock bedding is restored to horizontal, the dike strikes WNW and is subvertical. In total, more than 900 samples (cores and block samples) were collected from the five sections.

3. Laboratory methods

3.1. Paleomagnetism

Samples were processed in the paleomagnetism laboratories at both Nanjing University (NJU) and Yale University (Yale). The oriented samples were cut into cylindrical specimens of 2.5 cm in diameter and 2.2 cm in height, or ~1 cm thick discs. The thin disc-shaped specimens were prepared to be picked up by an automatic sample-changing system (Kirschvink et al., 2008) at Yale. Specimens were thermally demagnetized in 16–30 steps with increments of 30–50 °C for low temperatures (<300 °C) and 5–15 °C for high temperatures (>300 °C). Each specimen was thus heated until thoroughly demagnetized/unstable, as high as >680 °C. Most specimens were cooled in liquid nitrogen before thermal demagnetization, which can effectively remove the viscous remanence from multidomain (MD) magnetite (Halgedahl and Jarrard, 1995). Remanent magnetizations were measured using 2G-Enterprises DC-SQUID magnetometers housed in magnetically shielded rooms at both NJU and Yale, with reproducible results between the two laboratories. Magnetic remanence directions were fit using principal component analysis (Kirschvink, 1980), and site-mean directions were calculated with Fisher spherical statistics (Fisher, 1953). Software packages PMGSC (version 4.2) of R. Enkin, PaleoMac of Cogné (2003), and PaleoMag of Jones (2002) were used to implement the paleomagnetic data analysis and related figure productions.

3.2. Rock magnetism

In order to characterize magnetic mineralogy and better understand the properties of the remanent magnetizations, we carried out a suite of rock magnetic experiments on representative specimens (cap dolostone and sandstone). The experiments were conducted at both NJU and the Institute for Rock Magnetism, University of Minnesota. These rock magnetic experiments include: (1) anisotropy of magnetic susceptibility (AMS) determined by a KLY-3S kappabridge; (2) thermal–magnetic experiments made with an MFK1-FA kappabridge susceptibility meter coupled with a CS-4 furnace; (3) triaxially stepwise-thermal demagnetization of isothermal remanent magnetization (IRM, Lowrie, 1990) using an RF-SQUID rock magnetometer (2G-760) and an ASC TD-48 oven; (4) hysteresis loop parameters measured on a Vibrating Sample Magnetometer; and (5) low-temperature properties of room-temperature saturation isothermal remanent magnetizations (RT-SIRMs) during cooling (300 to 20 K) and warming (20 to 300 K), and SIRMs during warming (20 to 300 K) after field-cooling (FC) and zero-field-cooling (ZFC) with a Quantum Design Magnetic Properties Measurement System. Except for the AMS measurements performed at two laboratories, all the rest were carried out at the Institute for Rock Magnetism, University of Minnesota.

4. Results

4.1. Paleomagnetic results

4.1.1. Sections I and II

Sections *I* and *II* are close to each other, and located in the most northeastern part of our study area (Fig. 1b). The Sugetbrak

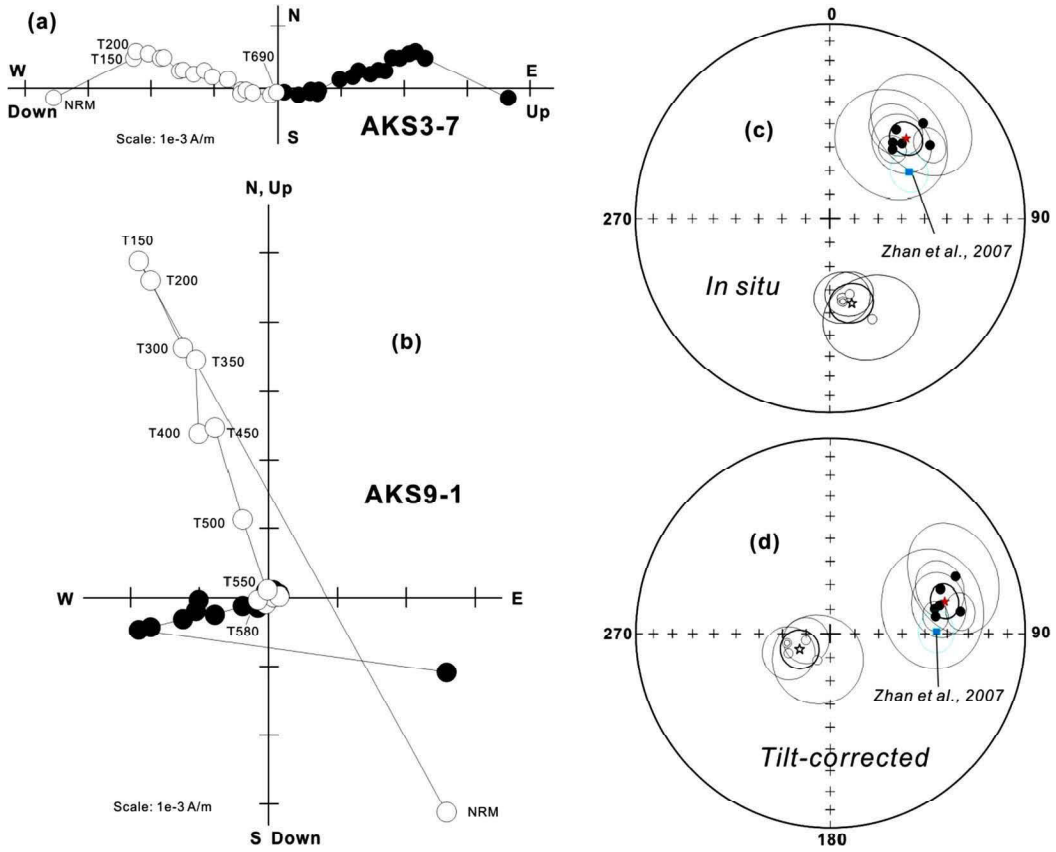

Fig. 2. Representative examples of progressive demagnetization (a–b) and mean-site directions (c–d) for the samples from sections *I* and *II*. Orthogonal projections are shown in stratigraphic coordinates. NRM, natural remanent magnetization; T100, demagnetization at 100 °C, etc. Mean directions are shown with stars and α_{95} confidence ovals; solid/open symbols mark the lower/upper hemispheric data.

Fm at these two sections is less than 400 m thick, and only one basalt layer is exposed (Fig. S1). We collected samples at seven sites from section *I* and ten sites from section *II*. About half of the specimens (sites) yield erratic directions (unstable or totally demagnetized at less than 200 °C), or directions of the recent Earth's field (Table 1) upon demagnetization. The remaining samples, after removing the viscous directions of present Earth's field (PEF) at low temperature (less than 200–300/350 °C), show characteristic remanent magnetizations (ChRMs) similar to those described by Zhan et al. (2007) from the same region: NE-down and SW-up directions (Table 1; Fig. 2). The site-mean direction for the NE-down group is $D_g = 043.6°$, $I_g = 42.9°$, $k_g = 96.8$, $\alpha_{95} = 6.8°$ in situ; $D_s = 074.4°$, $I_s = 39.1°$, $k_s = 109.9$, $\alpha_{95} = 6.4°$ after tilt correction ($n = 6$ sites). For the SW-up group, the site-mean direction is $D_g = 165.9°$, $I_g = -53.0°$, $k_g = 115.0$, $\alpha_{95} = 8.6°$ in situ; $D_s = 242.6°$, $I_s = -75.6°$, $k_s = 129.1$, $\alpha_{95} = 8.1°$ after tilt correction ($n = 4$ sites). Fold tests are inconclusive at the 95% confidence level for both the two groups (NE-down and SW-up; McElhinny, 1964). Also, the SW-up direction, in tilt-corrected coordinates (Fig. 2d), is broadly consistent with the results of Permian dikes in the region (Li et al., 1988).

4.1.2. Sections III, IV and V

Compared to the northeastern sections *I* and *II* of the study area (Fig. 1b), the Sugetbrak Fm strata are much better exposed and continuous at sections *III, IV*, and *V* (Figs. 1c and S1). Stratigraphic thickness at each is more than 400 m, and at least three basaltic layers within the sandstones have been recognized (Fig. S1; Turner, 2010; Zhu et al., 2011; B. Xu et al., 2013; Wen et al., 2015). The top layer basalts yielded the U–Pb zircon age of ca. 615 Ma (Fig. 1c; B. Xu et al., 2013). Moreover, the base of the Ediacaran Sugetbrak Fm, including the Marinoan-age glacial diamictites and post-glacial carbonate rocks (cap dolostones) from sections *III* and *V*, have been reported recently (Fig. 1c; Wen et al., 2015). Paleomagnetic results from the basal 'cap dolostones', the lower red sandstones and basalts, and the upper yellow–green siltstones are presented below.

(1) Basal 'cap dolostones' (section V). Multiple magnetic components of 'cap dolostones' (Fig. 3a and b) were revealed in the stepwise-thermal demagnetization from more than half of the sampling sites. Most of them show three components, termed 'LTC', 'MTC' and 'HTC', after low (below 300–350 °C), middle (350–550 °C), and high (up to 675 °C) temperature components, respectively. Some samples only exhibit two components of LTC and HTC, in which cases the HTC may persist to as high as 600 °C. The LTC is close to the PEF (Fig. 3a and b), and represents recent overprinting due to weathering and/or viscous behavior. The directions of MTC vary between different samples/sites, and are not similar to the PEF or the expected geocentric axial dipole (GAD) field, but are commonly intermediate between LTC and HTC, suggesting that it is a mixture of those two components. After removal of the LTC and MTC components, the magnetizations of HTC in the samples show linear trajectories to the origin, yielding the ChRMs with an unblocking temperature above 675 °C (Fig. 3a and b). These ChRMs are consistent among sites (Table 1) with a site-mean direction at: $D_g = 162.3°$, $I_g = 56.6°$, $k_g = 8.7$, $\alpha_{95} = 44.6°$; $D_s = 189.3°$, $I_s = 41.5°$, $k_s = 86.8$, $\alpha_{95} = 13.3°$ ($n = 3$ sites). The directions are more clustered after tilt correction than in *in situ* coordinates (Fig. 4a and b), indicating a positive fold test at the 95% confidence level ($k_s/k_g = 9.95$; McElhinny, 1964).

(2) Lower red sandstones and basalts. The majority of specimens show two or more stable magnetic components in the stepwise

Table 1
Paleomagnetic results in this study.

Section	Site	Lithology	S-Lat	S-Long	Strike	Dip	n/n_0	Polarity	D_g	I_g	D_s	I_s	k	α_{96}/MAD	Interpretation	Lab
I	AKS7	gray sandstone	41.0176	80.0386	47	35	7/9		171.4	−56.1	244.5	−70.7	30.5	11.1	P	NJU
	AKS6	gray sandstone	41.0177	80.0387	47	35	2/8		36.6	42.8	68.2	39.2	524.2	10.9	S–D	NJU
	AKS6	gray sandstone	41.0177	80.0387	47	35	2/8		165.8	−57.1	253.9	−79.5	685.0	9.6	P	NJU
	AKS5	red sandstone	41.0179	80.0386	52	34	4/7		6.0	49.4	56.6	63.1	6.0	41.1	Dispersed	NJU
	AKS4	red sandstone	41.0183	80.0383	52	34	2/7		39.6	48.3	76.7	44.4	119.4	23.1	S–D	NJU
	AKS3	red sandstone	41.0174	80.0367	52	34	7/7		42.0	50.6	80.7	44.6	111.2	5.7	S–D	NJU
	AKS2	red sandstone	41.0177	80.0364	52	34	0/8		–	–	–	–	–	–	Erratic	NJU
	AKS1	red sandstone	41.0176	80.0350	52	34	7/8		44.4	32.5	65.9	30.5	9.4	20.8	S–D	NJU
II	AKS16	yellow sandstone	40.9874	79.9921	58	35	0/7		–	–	–	–	–	–	Erratic	NJU
	AKS15	yellow sandstone	40.9876	79.9922	53	32	4/9		43.8	45.9	75.6	41.9	57.0	12.3	S–D	NJU
	AKS14	gray limestone	40.9878	79.9924	57	37	9/9		53.7	36.7	80.4	32.9	50.0	6.9	S–D	Yale
	AKS13	yellow sandstone	40.9879	79.9924	48	37	0/9		–	–	–	–	–	–	Erratic	Yale
	AKS12	yellow sandstone	40.9879	79.9924	48	37	0/11		–	–	–	–	–	–	Erratic	Yale
	AKS11	yellow sandstone	40.9880	79.9924	48	37	0/8		–	–	–	–	–	–	Erratic	NJU
	AKS10	red sandstone	40.9880	79.9924	52	40	0/10		–	–	–	–	–	–	Erratic	Yale
	AKS9	red sandstone	40.9880	79.9924	52	40	7/7		171.5	−54.5	257.4	−71.5	2590.0	1.2	P	NJU
	AKS8	red sandstone	40.9881	79.9924	52	40	2/10		157.4	−43.5	205.9	−77.7	179.1	18.8	P	NJU
	AKS2-17	basalt	40.9919	79.9919	57	44	8/8		13.8	38.5	61.8	55.3	417.3	2.5	Cenozoic	Yale
III	AD18	yellow sandstone	40.9147	79.8428	60	30	0/9		–	–	–	–	–	–	Erratic	Yale
	AD19	yellow sandstone	40.9151	79.8429	60	30	0/8		–	–	–	–	–	–	Erratic	Yale
	AD20	yellow sandstone	40.9157	79.8432	60	30	0/7		–	–	–	–	–	–	Erratic	Yale
	AD21	red sandstone	40.9168	79.8414	51	32	3/3	R	22.6	−69.2	347.1	−44.6	875.6	3.4	Primary	Yale
	BA1	basalt	40.9169	79.8413	54	32	0/11		–	–	–	–	–	–	Erratic	Yale
	AD22	red sandstone	40.9171	79.8400	51	32	7/7	R	34.5	−73.6	346.6	−50.3	11.2	17.3	Primary	Yale
	AD27	red sandstone	40.9171	79.8396	58	23	3/10		188.6	58.1	174.1	38.7	7.7	38.0	Dispersed	Yale
	AD23	red sandstone	40.9172	79.8392	58	23	2/8		66.8	33.4	79.9	27.0	7.1	72.4	Dispersed	Yale
	AD26	red sandstone	40.9172	79.8387	55	22	2/9	N	241.3	57.5	208.9	53.5	1186.7	5.1	Primary	Yale
	BA4	basalt	40.9175	79.8377	50	30	8/8	R	133.6	−61.0	28.1	−86.8	99.6	5.2	Primary	Yale
	AD24	red sandstone	40.9179	79.8382	49	30	7/10	R	73.2	−47.8	36.9	−51.2	9.1	19.4	Primary	Yale
	AD38	red sandstone	40.9180	79.8380	54	30	2/6		60.8	−37.0	38.5	−34.6	1.4	79.0	Dispersed	Yale
	AD37	red sandstone	40.9181	79.8377	72	35	9/10	R	221.9	−86.1	335.8	−56.8	9.8	16.2	Primary	Yale
	AD36	red sandstone	40.9182	79.8374	69	38	2/7	N	203.0	58.2	183.0	25.9	56.2	23.8	Primary	Yale
	AD35	red sandstone	40.9184	79.8371	68	30	4/12	N	171.9	69.9	164.2	40.3	11.6	24.1	Primary	Yale
	AD34	red sandstone	40.9185	79.8369	69	22	3/11		104.1	60.6	124.9	44.7	13.0	35.7	Dispersed	Yale
	BA5	basalt	40.9195	79.8355	77	24	0/10		–	–	–	–	–	–	Erratic	Yale
	BA6	basalt	40.9195	79.8354	77	24	0/8		–	–	–	–	–	–	Erratic	Yale
	AD25	red sandstone	40.9195	79.8353	77	24	12/12		25.3	2.3	28.5	20.8	36.5	7.3	Mesozoic	Yale
	AD33	red sandstone	40.9212	79.8376	77	24	4/11		239.4	33.6	227.2	23.7	3.6	44.3	Dispersed	Yale
	AD32	red sandstone	40.9219	79.8377			9/11		350.5	−12.8	0.6	−82.6	1.7	60.1	Soft-sediment fold	Yale
	AD31	red shale	40.9222	79.8388	69	27	9/14	R	64.1	−49.6	37.4	−41.0	12.8	14.1	Primary	Yale
	AD30	red sandstone	40.9223	79.8374	65	30	7/7	N	166.5	73.3	159.7	43.5	58.7	7.4	Primary	Yale
	AD29	red sandstone	40.9205	79.8313	75	27	7/10	R	73.6	−64.7	30.8	−53.0	6.3	23.8	Primary	Yale
	AD28	red sandstone	40.9206	79.8311	83	29	3/14	N	216.3	51.5	201.7	27.7	38.6	16.4	Primary	Yale
IV	WS7	red sandstone	41.0804	79.3593	258	39	3/7		90.1	31.5	64.2	33.1	59.5	16.1	S–D	NJU
	WS8	red sandstone	41.0804	79.3593	258	39	5/8		88.2	15.8	75.0	20.5	23.2	16.2	S–D	NJU
	WS9	yellow sandstone	41.0791	79.3615	243	38	4/8		175.4	−61.4	163.1	−25.2	29.6	17.2	P	NJU
	WS10	yellow sandstone	41.0789	79.3617	243	38	6/10		171.9	−58.3	162.2	−21.8	27.0	13.1	P	NJU
	WS11	yellow sandstone	41.0789	79.3617	243	38	6/8		3.3	62.3	348.7	26.7	140.9	5.2	PEF	Yale
	WS12	yellow sandstone	41.0788	79.3617	243	38	4/9		180.5	−45.3	172.8	−9.8	14.3	21.6	P	Yale
	WS13	green sandstone	41.0786	79.3622	248	37	5/7		209.0	−14.9	207.5	9.2	23.7	16.0	P	NJU
	WS14	green sandstone	41.0784	79.3628	248	37	4/8		206.1	−25.8	199.5	−0.4	33.2	16.2	P	NJU
	WS15	gray sandstone	41.0776	79.3657	252	36	8/10		277.0	−8.6	268.2	−19.0	2.9	39.6	Dispersed	Yale
	WS16	green sandstone	41.0776	79.3657	252	36	5/8		212.9	−24.7	206.2	−1.4	10.8	24.4	P	NJU
	WS17	green sandstone	41.0775	79.3658	243	40	3/7		212.0	−39.7	194.7	−14.9	20.7	27.8	Dispersed	NJU
	WS18	mafic dike	41.0774	79.3660	253	36	0/22		–	–	–	–	–	–	Erratic	NJU
	WS19	yellow sandstone	41.0774	79.3660	253	36	9/11		207.7	−44.8	193.3	−16.8	12.3	15.3	P	NJU
	WS20	gray sandstone	41.0773	79.3663	253	32	6/8		232.7	−69.4	194.7	−45.7	16.6	15.4	P	Yale

Table 1 (*continued*)

Section	Site	Lithology	S-Lat	S-Long	Strike	Dip	n/n_0	Polarity	D_g	I_g	D_s	I_s	k	α_{96}/MAD	Interpretation	Lab
	WS21	gray sandstone	41.0771	79.3664	258	34	8/14		95.7	−56.3	129.1	−38.3	4.8	25.5	Dispersed	Yale
	WS22	red sandstone	41.0769	79.3665	257	32	7/9	R	330.6	−5.7	325.7	−35.2	7.5	21.6	Primary	Yale
	WS23	red sandstone	41.0768	79.3665	252	38	2/9	R	12.3	−19.0	27.7	−51.3	180.1	13.2	Primary	Yale
	WS24	gray sandstone	41.0765	79.3667	268	44	1/11	N	164.2	8.3	155.8	50.2		8.5	Primary	Yale
	WS25	gray sandstone	41.0765	79.3667	268	47	14/14	R	340.3	23.7	340.8	−20.5	313.6	2.2	Primary	Yale
	WS26	basalt	41.0765	79.3667	268	47	5/8	R	336.8	24.3	337.5	−19.9	36.9	12.8	Primary	Yale + NJU
	WS27	gray sandstone	41.0765	79.3667	268	47	7/8	R	341.6	20.6	341.1	−23.5	252.9	3.5	Primary	Yale
	WS28	basalt	41.0765	79.3667	268	47	0/11		–	–	–	–	–	–	Erratic	Yale
	WS29	red sandstone	41.0765	79.3667	268	47	5/10	R	355.4	−9.3	350.5	−55.8	9.5	23.2	Primary	Yale
	WS30	red sandstone	41.0765	79.3667	268	47	4/7		22.9	12.6	26.3	−29.9	5.7	42.4	Dispersed	NJU
	WS31	red sandstone	41.0753	79.3681	255	39	2/8		246.4	−35.6	224.2	−23.7	13.5	74.4	Dispersed	NJU
V	AK6-40	purple sandstone	40.8270	79.2936	101	30	8/8		80.3	26.9	97.7	33.1	195.3	3.7	S–D	Yale
	AK6-39-2	basalt	40.8271	79.2936	101	30	6/6	N	97.4	32.5	115.7	29.2	248.8	3.9	Primary	Yale
	AK6-39-1	basalt	40.8271	79.2936	101	30	8/8	N	130.4	47.5	148.9	28.0	109.6	5.0	Primary	Yale
	AK6-38	basalt	40.8275	79.2936	101	30	9/9	R	5.9	−76.4	8.9	−46.4	480.4	2.2	Primary	Yale
	AK6-37	basalt	40.8280	79.2939	101	30	0/11		–	–	–	–	–	–	Erratic	Yale
	AK6-36	pink-purple sandstone	40.8284	79.2940	101	30	5/7	N	92.3	57.8	134.7	50.5	78.7	7.8	Primary	Yale
	AK6-35	basalt	40.8293	79.2927	93	32	7/7	N	117.6	53.4	142.4	33.2	106.0	5.5	Primary	Yale
	AK6-34	sill	40.8313	79.2918	93	32	0/7		–	–	–	–	–	–	Erratic	Yale
	AK6-33	red sandstone	40.8319	79.2924	88	46	8/8	R	143.4	−76.9	10.0	−54.2	20.6	11.6	Primary	Yale
	AK6-32	red sandstone	40.8322	79.2926	88	46	5/10	R	174.2	−64.8	1.5	−69.1	10.5	21.9	Primary	Yale
	AK6-30	red sandstone	40.8328	79.2928	88	46	7/7	R	223.6	−63.5	317.6	−59.9	13.3	15.8	Primary	Yale
	AK6-29	sill	40.8334	79.2925	82	48	0/13		–	–	–	–	–	–	Erratic	Yale
	AK6-28	sill	40.8336	79.2934	99	37	4/6		64.9	8.6	75.7	26.7	794.4	2.8	S–D	Yale
	AK6-27	red sandstone	40.8347	79.2955	94	30	8/9		22.8	55.2	77.0	78.7	7.5	20.1	PEF	Yale
	AK6-16	mafic dike	40.8351	79.2974			8/14		193.9	−40.0	205.4	−69.1	30.8	9.5	P	Yale
		baked contact sandstone	40.8351	79.2974	94	30	11/11		200.2	−59.0	274.2	−81.8	66.4	5.4	P	Yale
		baked boundary	40.8351	79.2974	94	30	3/4		129.5	−18.0	116.7	−32.9	12.8	36.0	Dispersed	Yale
		country sandstone	40.8351	79.2974	94	30	10/10	N	159.2	60.6	170.0	32.2	8.4	16.8	Primary	Yale
	AK6-15	red sandstone	40.8357	79.2987	84	36	4/11		102.2	−27.6	80.6	−32.8	17.3	19.5	O	Yale
	AK6-14	red sandstone	40.8358	79.2987	94	29	4/8		35.4	−80.0	12.2	−52.2	2.9	51.3	Dispersed	Yale
	AK6-13	red sandstone	40.8359	79.2987	94	32	12/12	N	192.6	63.7	188.2	31.9	15.9	10.7	Primary	Yale
	AK6-12	red sandstone	40.8361	79.2987	85	35	15/17	N	88.0	66.8	138.8	47.7	7.3	14.7	Primary	Yale
	AK6-50-3	red siltstone	40.8385	79.3093	105	34	12/12	R	285.8	−66.8	337.7	−49.4	118.3	3.8	Primary	Yale
	AK6-50-2	red siltstone	40.8386	79.3094	105	34	10/10	R	338.5	−65.5	357.6	−34.6	35.8	7.8	Primary	Yale
	AK6-50-1	red siltstone	40.8386	79.3094	105	34	10/12	R	309.1	−65.1	344.4	−41.0	20.1	10.4	Primary	Yale
	AK6-3	sill	40.8403	79.2965	103	25	10/10		94.1	−2.5	93.9	1.5	6.7	18.9	S–D	Yale
	AK6-9	cap-dolostone	40.8428	79.2890			3/11		141.7	18.7	165.2	39.9	4.7	64.7	Dispersed	Yale
	AK6-8	cap-dolostone	40.8431	79.2887	Individual beddings		8/10	N	156.5	28.8	183.2	38.8	7.0	20.9	Primary	Yale
	AK6-7	cap-dolostone	40.8444	79.2907			4/14		219.5	61.2	194.1	58.4	4.4	49.9	Dispersed	Yale
	AK6-6	cap-dolostone	40.8438	79.2914			5/11		0.1	64.8	10.7	46.3	12.8	22.2	PEF	Yale
	AK6-5	cap-dolostone	40.8387	79.3096			4/7		274.3	54.5	247.4	58.2	8.6	33.4	Soft-sediment fold	Yale
	AK6-4	cap-dolostone	40.8387	79.3095	130	38	11/28	N	127.7	74.0	194.7	49.8	6.3	18.7	Primary	Yale
	AK6-2	cap-dolostone	40.8404	79.2967	102	25	13/14	N	192.4	60.6	192.2	35.6	26.5	8.2	Primary	Yale
$Mean_N$							**16**	**N**	**155.9**	**62.2**			**7.8**	**14.2**		
											167.7	**41.6**	**13.1**	**10.6**		
$Mean_R$							**20**	**R**	**359.5**	**−62.8**			**3.0**	**23.2**		
											354.3	**−49.5**	**13.5**	**9.2**		
Mean							**36**	**N + R**	**167.3**	**63.0**			**4.1**	**13.5**		
											171.2	**46.0**	**13.2**	**6.8**		
Paleomagnetic pole									**−21.1N, 87.4E, $dm/dp = 8.7/5$**							

Notes: S-Lat/S-Long, latitudes and longitudes of sampling sites; n/n_0, number of specimens in calculation/number of specimens demagnetized in each site; N and R, normal and reversed polarities; D_g, I_g, D_s and I_s, declination and inclination in geographic and stratigraphic coordinates, respectively; k, precision parameter; α_{95}, 95% confidence ovals; MAD, maximum angular deviation; dm/dp, the semi-axes of the ellipse of confidence for a paleomagnetic pole; O, S, D and P, remagnetization ages in Ordovician, Silurian, Devonian and Permian; Dispersed, mean directions with $\alpha_{95} > 25°$. Strike/Dip, the strike and dip of the bedding attitudes following the right hand rule. All angles are in degrees.

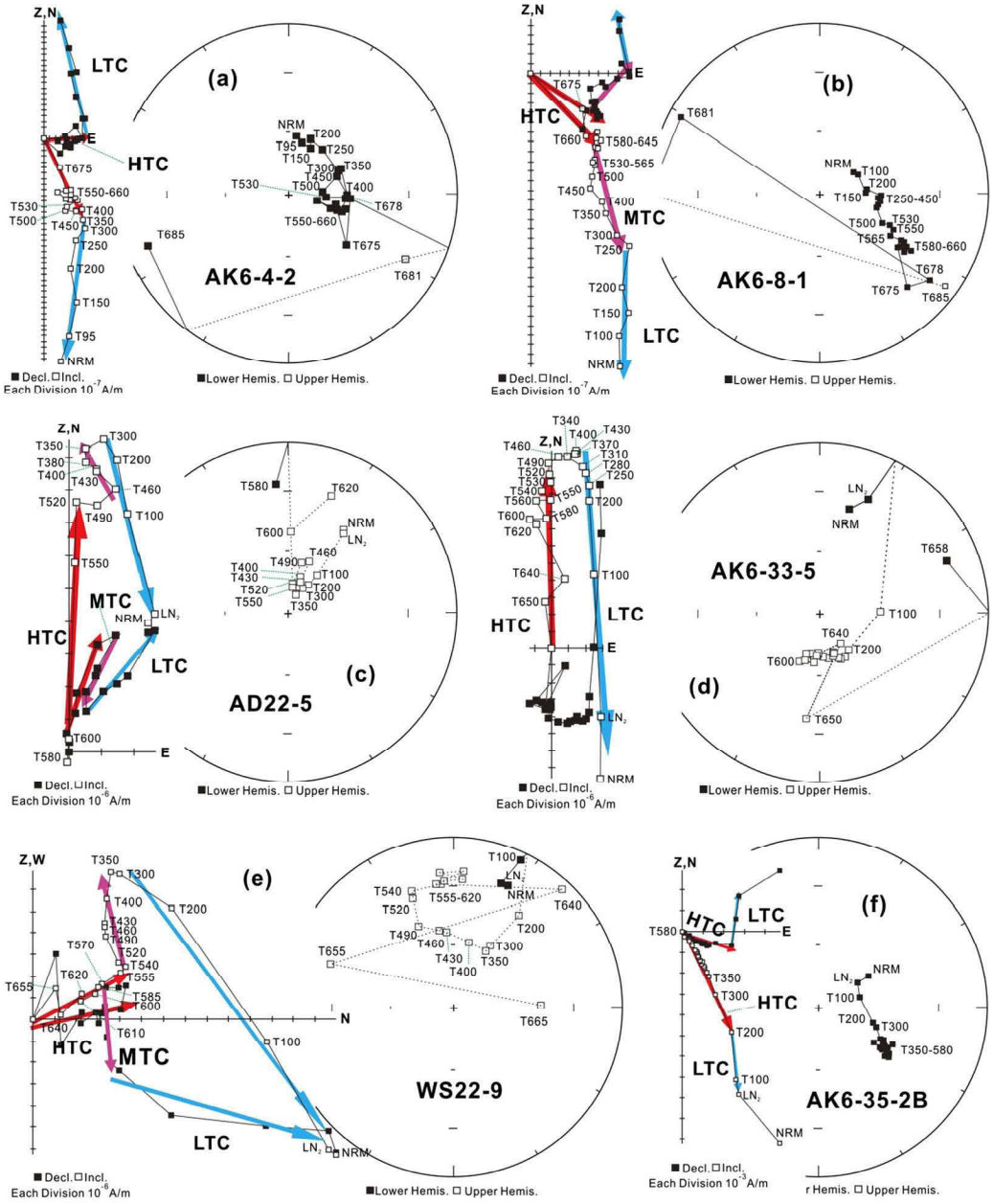

Fig. 3. Typical orthogonal and equal-area projections of demagnetization behavior for the samples from sections *III*, *IV* and *V*, showing the multiple components. Representative samples include cap carbonates (a–b), redbeds (c–e) and basalts (f). NRM, natural remanent magnetization; LN_2, samples cooled in liquid nitrogen; T100, demagnetization at 100 °C, etc. All plots are in geographic coordinates. The HTCs linearly decaying to the origins represent the ChRMs, and the erratic points after ChRMs are not shown in the orthogonal vector projections.

demagnetization (Fig. 3c–f). Their LTCs are commonly close to the PEF, while MTCs show a variable remagnetization of non-GAD field (commonly directed SSW and Up, similar to that found in sections *I* and *II*). The HTCs, linearly decaying toward the origins at 580 °C or above 650 °C (Fig. 3c–f), define the ChRMs and are isolated from 33 sites (Table 1). Among these sites, 27 sites are from sandstones and yield a mean direction of $D_g = 177.4°$, $I_g = 63.8°$, $k_g = 4.2$, $\alpha_{95} = 15.5°$, and $D_s = 173.6°$, $I_s = 46.7°$, $k_s = 15.9$, $\alpha_{95} = 7.2°$; while the remaining 6 sites are obtained from basalt layers and yield a mean direction of $D_g = 129.9°$, $I_g = 55.3°$, $k_g = 2.9$, $\alpha_{95} = 48.1°$, and $D_s = 149.7°$, $I_s = 42.3°$, $k_s = 7.2$, $\alpha_{95} = 26.8°$. Since the two means of the tilt-corrected directions are close to each other, all the 33 sites are combined together in the following analysis. The ChRMs include normal and reversed polarities (Fig. 4c and d), and pass a reversal test at the 95% confidence level (class C; McFadden and McElhinny, 1990). An average site-mean direction of the combined polarities is at: $D_g = 168.0°$, $I_g = 63.7°$, $k_g = 3.9$, $\alpha_{95} = 14.7°$, and $D_s = 169.2°$, $I_s = 46.3°$, $k_s = 12.6$, $\alpha_{95} = 7.3°$ with $n = 33$ sites. Both the fold tests of McElhinny (1964) and Enkin (2003) give positive results for these ChRMs at the 95% confidence level.

(3) Upper sand- or siltstones (*section IV*). Unlike the lower red sandstones, the upper sandstones/siltstones of Sugetbrak Fm show a less stable demagnetization behavior. Several sites of yellow–green sandstone possess no stable magnetization (Table 1) after removing the viscous directions of PEF at less than 200 °C (more than 90% magnetic contribution of goethite), and the rest yield highly variable ChRMs, including the NE-down/SW-up directions broadly coincident with those from sections *I* and *II* (Table 1). These ChRMs become more dispersed after tilt correction (Fig. 4e and f), but the fold test is inconclusive at the 95% confidence level (McElhinny, 1964).

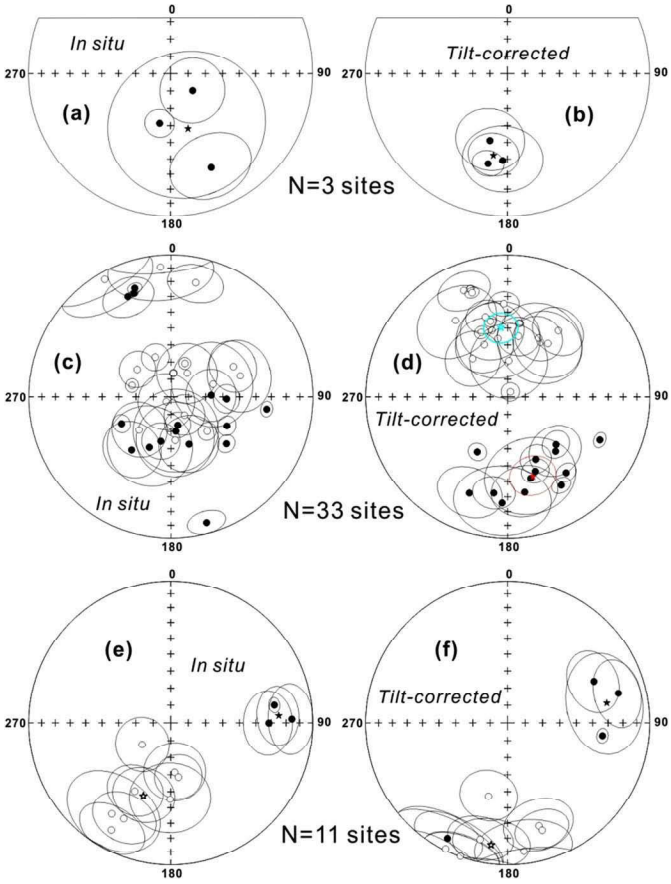

Fig. 4. Equal-area stereographic projections of mean-site directions for the Ediacaran strata at sections *III*, *IV* and *V*. Directions are shown in both geographic (left; in situ) and stratigraphic (tilt-corrected) coordinates. (a–b) The basal 'cap dolostones'; (c–d) the lower red sandstones and basalts; (e–f) the upper sand- or siltstones. Mean directions from each polarity are shown with stars and α_{95} confidence ovals; solid/open symbols mark the lower/upper hemispheric data.

4.2. Rock magnetic results

The AMS data of the representative samples of sandstones from the five sections show low anisotropy ($Pj < 1.03$). Fig. 5 shows that the maximum axes mainly lie within the bedding plane and minimum axes are perpendicular to the plane, suggesting a sedimentary or depositional fabric. However, the rest of the rock magnetic experiments were only conducted on the 'cap dolostone' and red sandstone samples of the lower Sugetbrak Fm which possess stable magnetic components. Based on their different characteristics, the results are described separately.

4.2.1. 'Cap dolostones'

The representative cap dolostone samples show slightly wasp-waisted shape of "fat" or "pot-bellied" hysteresis loops (Fig. 6a). They reach magnetic saturation at about 1.4 T and have relatively high coercive force (Hc, 255–527 mT) and coercivity of remanence (Hcr, 602–698 mT) values, suggesting the dominance of magnetically 'hard' minerals. On the FC-ZFC and RTSIRM curves of low-temperature measurements (Fig. 6d), large remanence decrease below ~260 K characterizes the Morin transition of hematite (Morin, 1950). The presence of hematite can be further confirmed by both thermal–magnetic experiments and 3-axis thermal demagnetization of IRMs. The susceptibility shows very similar variation trends during heating and cooling (Fig. 6e): rapid decrease in susceptibility occurs at above 650 °C (hematite). As for the triaxially thermal demagnetization, samples were sequentially magnetized along *Z*-, *Y*-, and *X*-axis (three orthogonal axes) at fields of 1.0 T, 0.4 T and 0.12 T, respectively. Fig. 6f shows that the magnetization is mainly contributed by minerals with coercivity of 0.4–1.0 T, and a very small amount is from low-coercivity (below 0.4 T) phases. Meanwhile, the unblocking temperature for the high-coercivity components (*Z*-axis; Fig. 6f) is at ca. 680 °C.

4.2.2. Sandstones

Unlike the 'cap dolostones', the red sandstones exhibit more "wasp-waisted" hysteresis loops (Fig. 6b and c), indicating a mixture of coercive/grain-size minerals. The high-coercivity minerals in samples are demonstrated by the high field (>1.2 T) of magnetic saturations. On the curves of low-temperature measurements, a rapid drop at 120 K and a slight decrease at 260 K can be observed (Fig. 6g), suggesting the presences of magnetite and hematite (Verwey, 1939; Morin, 1950). These magnetic minerals also can be recognized by both thermal magnetic measurements and triaxial thermal demagnetization of IRMs. As shown in Fig. 6h and i, the magnetization decreases corresponding to magnetite (about 580 °C) and hematite (about 680 °C) can be observed on the curves.

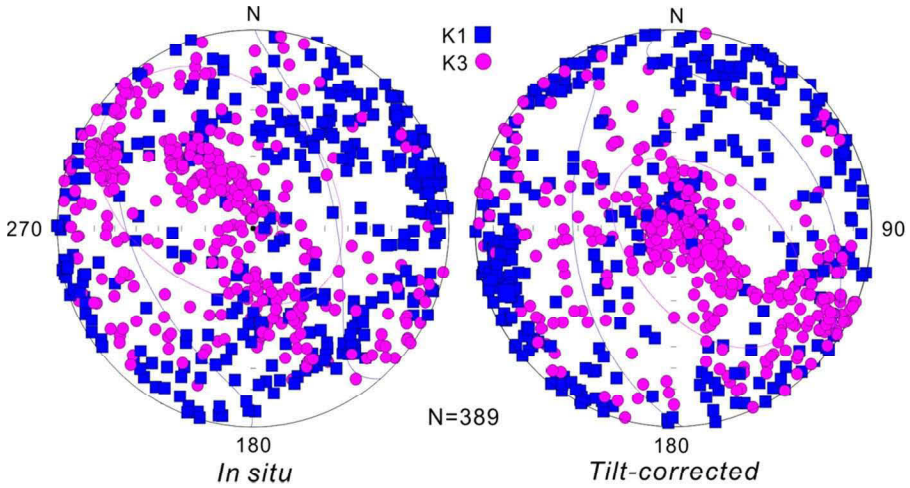

Fig. 5. Anisotropy of magnetic susceptibility (AMS) data of the representative samples in geographic (left) and stratigraphic (right) coordinates. K1/K3, maximum/minimum axes.

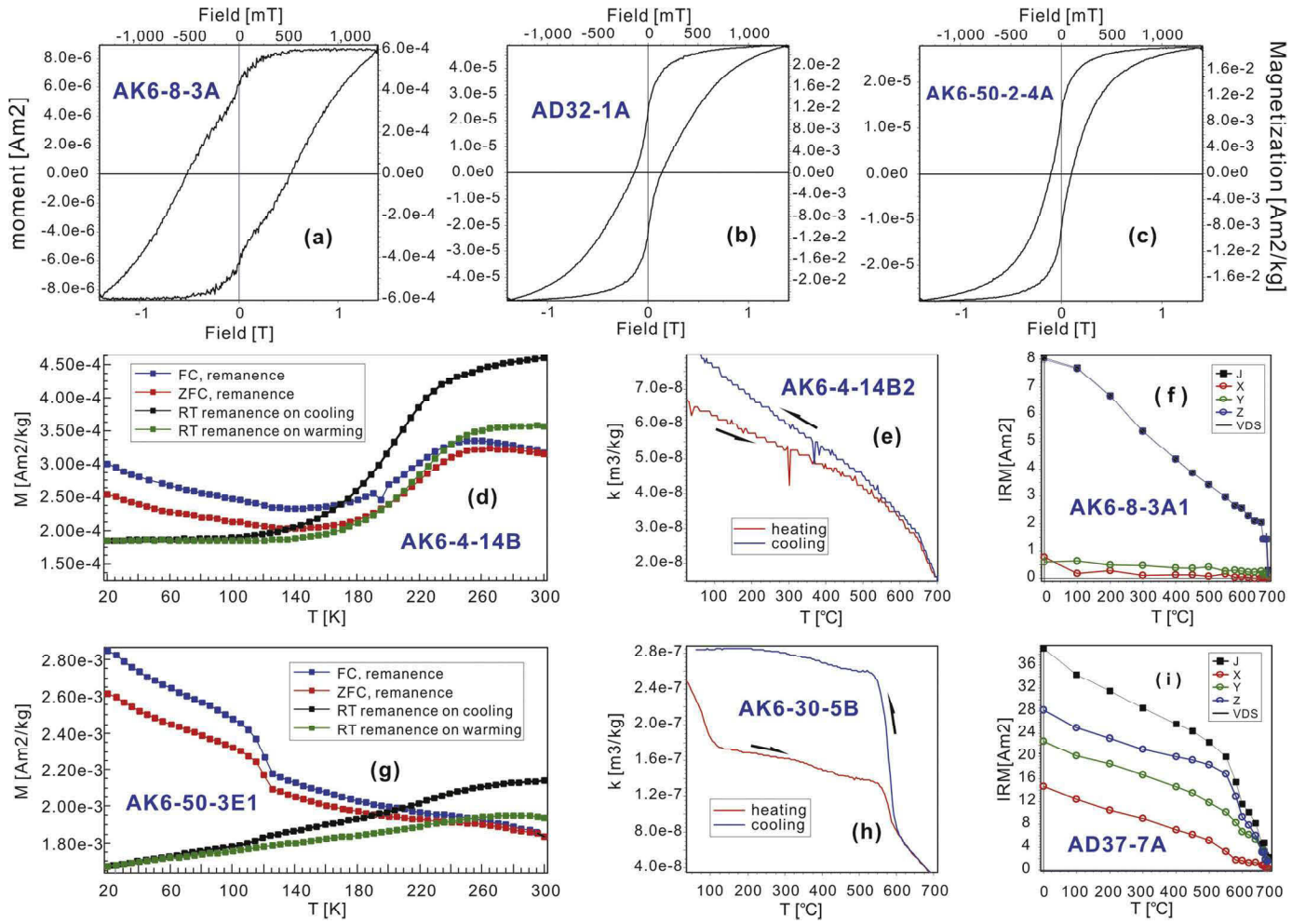

Fig. 6. Representative examples of rock magnetism. (a–c) Hysteresis loops; (d and g) remanence curves of low-temperature measurements; (e and h) thermal–magnetic properties; (f and i) triaxially thermal demagnetization of isothermal remanent magnetizations. Note the different units on left/right sides for the hysteresis loops.

5. Discussion

5.1. Timing of the remanence acquisition

5.1.1. Sections I, II and Upper Sugetbrak Fm at III, IV and V

As mentioned above, samples from the sections *I* and *II*, as well as from the upper sand- and siltstone across the whole study area (*III* and *IV*), show a less stable demagnetization behavior, and yield two non-antipolar ChRMs: NE-down and SW-up directions. Also, the NE-down group commonly shows inconclusive regional tilt tests, and the SW-up directions are broadly coincident with those from the Permian dikes in Tarim (Li et al., 1988). All these characteristics suggest that these samples appear to have been extensively remagnetized, and the SW-up directions are probably Permian in age. As for the NE-down group, including the data of Zhan et al. (2007), a paleomagnetic pole corresponding to the directions is calculated: $\lambda = 22.8°$N, $\varphi = 161.0°$E, $A_{95} = 6.2°$. In a comparison of this pole with the compilation of Phanerozoic paleomagnetic poles from the Tarim Block (Table S1), it is very close to the Silurian and Devonian poles (Fig. 7a); this suggests the occurrence of remagnetization during this time, perhaps associated with coeval magmatism in northern Tarim (e.g., Ge et al., 2014). Therefore, these paleomagnetic data and the similar ChRMs of Zhan et al. (2007) obtained from the same region (*I* and *II*) are excluded from further discussion, and their hypothesized remagnetization ages are assigned in Table 1.

5.1.2. Lower Sugetbrak Fm at sections III, IV and V

According to the magnetic directional analysis above, the lower Sugetbrak Fm ('cap dolostone', red sandstone and basalts) in the most southerly part (sections *III*, *IV* and *V*) of the Aksu–Wushi area (Fig. 1b) shows more stable and coherent directions. A series of stability tests were carried out to constrain the age of the ChRMs. Two soft-sediment folds within the basal 'cap dolostone' (AK6-5, section *V*) and red sandstone (AD32, section *III*) were sampled from both limbs of each fold (Fig. S2). Four out of 7 samples from the soft-sediment fold of AK6-5 yield stable ChRMs (Tables 1 and S2). The ChRMs become slightly clustered after tilt correction with the $k_s/k_g = 8.6/7.0$, and the maximum grouping occurs at 54.22% ± 86.31% untilting, suggesting an inconclusive fold test (Enkin, 2003). Nine of 11 ChRMs (Tables 1 and S2) from the other fold at AD32 are less clustered in stratigraphic coordinates than in geographic coordinates, with the k_s/k_g ratio of 1.7/6.0. Meanwhile, the optimal untilting for the concentration is achieved at −6.85% ± 45.88%, and a negative fold test is implied (Enkin, 2003). Negative soft-sediment fold tests, however, do not preclude a remanence age that is "primary" for the purpose of tectonic reconstructions; for example, an early diagenetic crystallization-remanent magnetization (CRM) held by hematite is common in red sedimentary rocks. Consequently, according to these tests it is not clear whether the magnetic remanence represents Tarim paleogeography in early Ediacaran time.

The variable bedding attitudes across the study area (ca. 30–40° dip toward to SE and NW; Figs. 1c and S1) allow us to conduct a

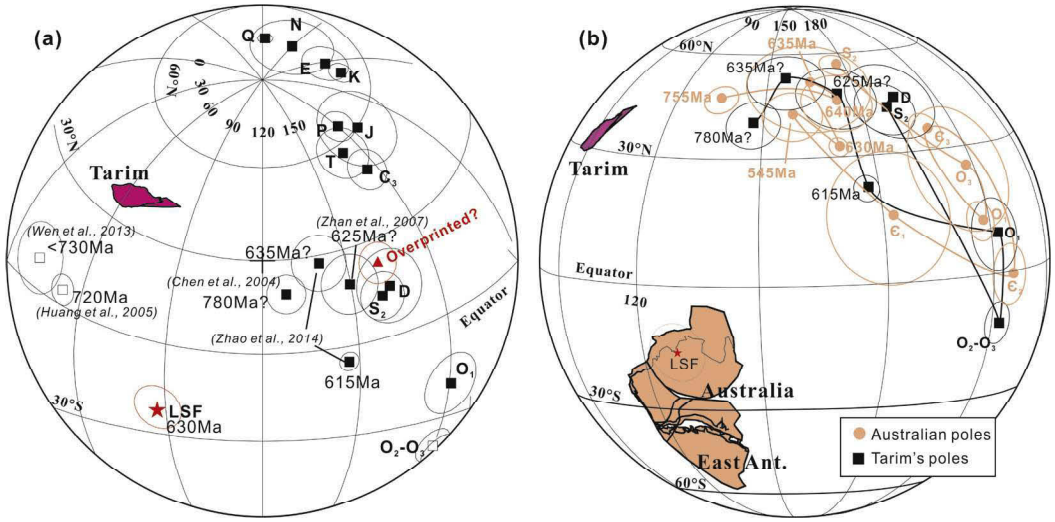

Fig. 7. (a) Comparison of the likely primary (star) and remagnetized (triangle) paleomagnetic poles from the Ediacaran Sugetbrak Formation with the compilation of Phanerozoic paleopoles from the Tarim Block (see Table S1), showing the Neoproterozoic paleopoles published (Chen et al., 2004; Huang et al., 2005; Zhan et al., 2007; Wen et al., 2013; Zhao et al., 2014). (b) Invalid connection of Tarim and Australia by rotating Tarim around an Euler pole (45.9°S, 277.6°E, angle −43.4°) to fit the Neoproterozoic–early Paleozoic paleopoles from the two cratons proposed by Zhao et al. (2014) (their cartoon reconstruction incorrectly claims that such a rotation brings those cratons into direct contact). O, S, D, C, P, T, J, K, E, N and Q, represents Ordovician, Silurian, Devonian, Carboniferous, Permian, Triassic, Jurassic, Cretaceous, Paleogene, Neogene and Quaternary, respectively. Solid/open symbols mark the front/back projections.

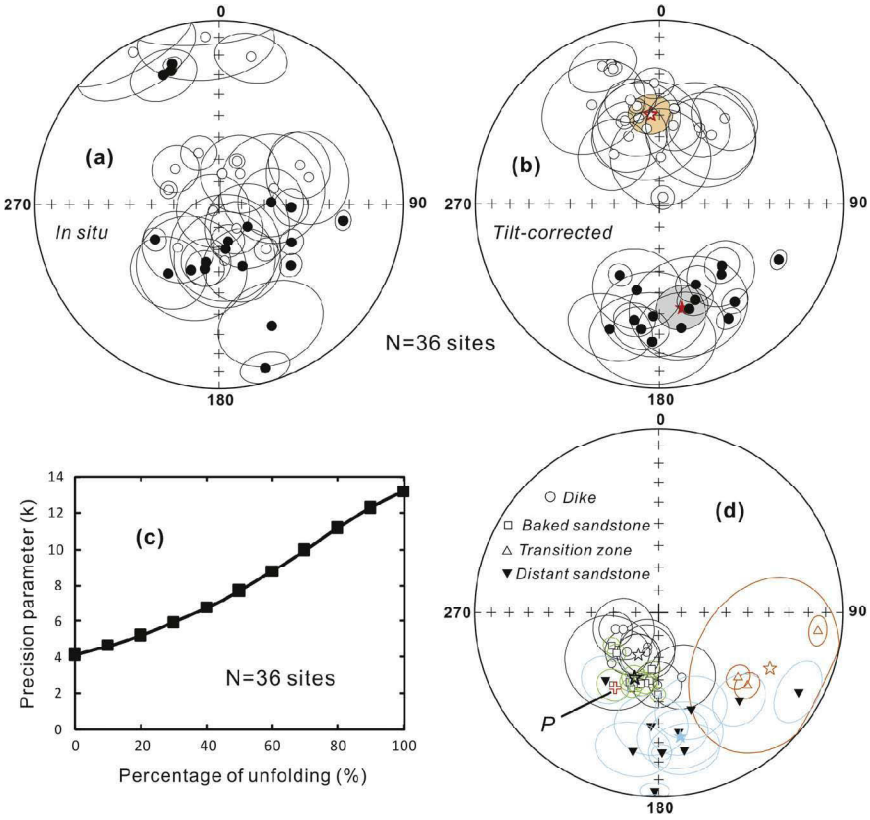

Fig. 8. Paleomagnetic directions and field stability tests for the Ediacaran strata in NW Tarim. (a–b) Equal-area stereographic projections of each site in both geographic and stratigraphic coordinates; (c) progressive regional unfolding, showing a significant clustering of directions after 100% untilting; (d) inverse baked-contact test (shown in tilt-corrected coordinates), showing individual sample directions and difference in mean directions for different sampling zones relative to a likely Permian mafic dike. Mean directions from each polarity are shown with asterisks and α_{95} confidence ovals; *P*, expected direction calculated (reference point at 41°N, 79°E) from the mean-Permian pole of Tarim (Table S1). Solid/open symbols mark the lower/upper hemispheric data.

regional tilt test. The combined ChRM dataset from the cap carbonate and redbeds of the lower Sugetbrak Fm is much better concentrated after tilt correction (Fig. 8a–c) with the k_s/k_g ratio of 13.5/4.1, and a positive fold test is achieved at the 95% confidence level (Enkin, 2003). Deformation in the Aksu–Wushi region is mainly Cenozoic in age (Turner et al., 2010). However, a positive (inverse) baked-contact test is observed at site AK6-16 (Fig. S1). Samples drilled from this site can be categorized into four outcrop groups – A, B, C and D (Fig. 8d; Table 1). Samples in Group A were drilled from the mafic dike and yield well-grouped ChRMs of SW-upward directions. These directions are similar to those of the Permian dikes near our study area (Li et al., 1988) and overlap

the expected direction (Fig. 8d) calculated from the mean-Permian pole of Tarim (Table S1). Samples in Group B are baked sandstone within 10 cm from the contact, and show the same remanence direction as that of the dike. A little further (ca. 30–50 cm) from the contact are the samples of Group C. These samples display less clustered directions of southeast declinations and upwards inclinations; the directions are not easily explained but could result from varying degrees of mixing of high- and low-stability components of magnetization. Samples in group D are further away (>50 cm) from the contact, in unbaked host sandstone, and show a coherent SSE-down direction that is similar to results from the surrounding sites. Consequently, these data indicate a passage of the (inverse) baked contact test for the lower Sugetbrak Fm remanence.

Consistency of ChRM polarity across lithostratigraphically defined intervals constitutes an informal stability test on the age of magnetization. In the Sugetbrak Fm at southerly sections, the remanence polarity zones are "chunky" and are broadly consistent from section to section; namely, although lithostratigraphy varies across the region, the mid-Sugetbrak transition from red to yellow (reduced, lacustrine?) sedimentation lies within a reversed polarity zone. The highly clustered directions of NNW-up and nearly antipodal SSE-down in stratigraphic coordinates (Fig. 8b) generate a positive reversal test of class C (McFadden and McElhinny, 1990).

In summary, these stability tests suggest that the magnetic remanence of the lower Sugetbrak Fm was acquired prior to Permian time, and likely syn- or post-soft-folding, i.e., close to the time of deposition. Additional evidence in favor of the essentially primary origin for the magnetic remanence includes the reliable magnetic minerals (magnetite and hematite) and the weak anisotropy degree ($Pj < 1.03$) of AMS. An overall mean direction for the lower Sugetbrak Fm throughout the three sections was calculated at: $D_g = 167.3°$, $I_g = 63.0°$, $k_g = 4.1$, $\alpha_{95} = 13.5°$, and $D_s = 171.2°$, $I_s = 46.0°$, $k_s = 13.2$, $\alpha_{95} = 6.8°$ with $n = 36$ sites (Table 1), corresponding to a new paleopole 'LSF' (lower Sugetbrak Fm) at $\lambda = 21.1°$S, $\varphi = 87.4°$E, $A_{95} = 7.0°$ with a paleolatitude of $27.4 \pm 5.6°$. This new paleopole is dissimilar to all Phanerozoic results from Tarim craton (Fig. 7a), further corroborating its reliability. Because the lower Sugetbrak Fm is sandwiched between the underlying Marinoan-age (ca. 640 Ma) glacial diamictite and a ca. 615 Ma basalt layer near the top as described above, the age of this paleopole is estimated to be ~625 Ma.

5.2. Paleogeographic implications

If there is a 'missing-link' continental block to fill the gap between Australia–East Antarctica and Laurentia within Rodinia, a candidate craton must adhere to two key requirements: (1) geological link for both sides, plus a Rodinia-forming orogen; and (2) paleomagnetic constraints. As for the first aspect, recently, a Mesoproterozoic–early Neoproterozoic (1.1–1.0 Ga) orogenic belt, i.e., Grenville-age suture, across the central Tarim has been revealed recently by a comprehensive study of deep drilling in central Tarim (Fig. 1a; Z.Q. Xu et al., 2013). Granodiorite and diorite samples from the drilling core in central Tarim show geochemical signatures of calc-alkaline I-type granites, and yield hornblende $^{40}Ar/^{39}Ar$ isochron ages of $933.8 \pm 6.8/892.2 \pm 32.7$ Ma and 1199.4 ± 6.4 Ma, respectively (Z.Q. Xu et al., 2013 and references therein). Along that E–W trending belt in the central part of Tarim, there is also a significant gravity-magnetic anomaly (e.g., Jia et al., 2004; Guo et al., 2005), and ca. 0.94–0.90 Ga S-type granitoids outcropped in Altyn Tagh (e.g., Wang et al., 2013). The basement rocks of both sides contain vestiges of an Archean–Paleoproterozoic tectonic history (Fig. 1a; Z.Q. Xu et al., 2013 and references therein). Northern Tarim has an Archean–Paleoproterozoic (ca. 2.8–2.5 Ga) continental nucleus, while Southern Tarim is characterized by slightly younger ages (ca. 2.4–2.2 Ga). These age provinces could satisfy a "missing-link" position between Laurentia and Australia in Rodinia. The older Archean rocks of northern Tarim could correlate with the Archean cratons in western Laurentia: the Medicine Hat, Clearwater and Grouse Creek blocks of northwestern United States, and Hearne Craton to the north in adjacent Canada (e.g., Foster et al., 2006; Vervoort et al., 2016). Binding these Archean nuclei together, the Paleoproterozoic (2.0–1.8 Ga) igneous/metamorphic events in N-Tarim (Fig. 1a) are coincident with the widespread ca. 1.9–1.8 Ga magmatism in western Laurentia (Vervoort et al., 2016). Meanwhile, early Paleoproterozoic ages of 2.4–2.2 Ga in southern Tarim could correspond to various terranes of the same age interval in the Mawson continent (reviewed by Payne et al., 2009). If these correlations are correct, the Grenville-age orogen in the center of Tarim craton could have acted as the Rodinia-forming suture between Laurentia and Australia. In addition, the suture seems to extend into circum-Tarim terranes as well (Fig. 1a): Kunlun and Quanji (Lu et al., 2008), Altyn–Qaidam–Qilian area (e.g., Song et al., 2012), and central Tianshan, as suggested by detrital zircon ages (e.g., Ma et al., 2012). The aggregate dataset suggests a larger original area of 'Greater Tarim', now distinguished as central Asian terranes that collectively could have lain in an alternative "missing-link" position at central Rodinia. For simplicity in our illustration of Figs. 9 and 10, the Tarim block only extends to its east, Quanji–Alxa block (Fig. 1a; Lu et al., 2008), which is restored ca. 400 km along the AltynTagh fault after Yue et al. (2001).

Following culmination of the Grenville-age orogeny, Neoproterozoic rift-related records were also well developed in Tarim Block (e.g., Lu et al., 2008; Zhang et al., 2012), which can be correlated with both sides of the modified "missing-link" assemblage proposed herein (Fig. 9a). In previous studies, the breakup of Rodinia has been attributed to multiple episodes of mantle plume impingement, i.e., ca. 820–800 Ma and ca. 780–730 Ma (e.g., Li et al., 2003, 2008). As shown in Fig. 9b, the numerous igneous episodes in Tarim (Xu et al., 2005, 2009; Lu et al., 2008; Zhang et al., 2012) can reconcile the mismatching of ages on thermal events in central and southeastern Australia (Sun and Sheraton, 1996; Wingate et al., 1998) versus western Laurentia (Harlan et al., 2003; Denyszyn et al., 2009).

In this model, the position of South China can still be considered uncertain, and we discuss two alternatives. If it occupied a position adjacent to eastern Australia as previously proposed (e.g., Li et al., 1995, 2008), then the Tarim Block together with South China would have constituted a combined "missing-link" role (Figs. 9 and 10a). The similarity in Neoproterozoic geological history of these two cratons has been extensively discussed by Lu et al. (2008) and shown in Fig. 9a, while diachroneity between the older Tarimian orogeny and the younger Sibao orogen (see above) would need to be attributed to either incomplete understanding of the former, or a lengthy zipper-like suturing evolution toward the latter. Detrital zircon age spectra are similar between northern Tarim and Cathaysia during most of Proterozoic time (Shu et al., 2011), thus providing some support for the combined 'missing-link' model. The initial breakup of Rodinia occurred after Sturtian glaciation (<730 Ma) based on the tectonostratigraphic and paleomagnetic synthesis of both Australia and Laurentia (Li and Evans, 2011). Consequently, the Sturtian-age Qiaoenbrak Fm pole of Tarim (QF; Wen et al., 2013) could provide good paleomagnetic control for the reconstruction, and a revised configuration following Li and Evans (2011) is produced by placing Tarim in between (Fig. 10a). In such a configuration, the ca. 740 Ma Baiyisi Fm pole (BF; Huang et al., 2005) and the <730 Ma QF pole of Tarim are coincident with the ca. 720–750 Ma poles of both Australia and Laurentia (Fig. 10a; Table 2); the 755 Ma MDS (Mundine Well Dike Swarm) pole from Western Australia has been restored to northern Australia around an Euler pole (20°S, 135°E, angle 40°), and one optional position for South China is shown using the <750 Ma

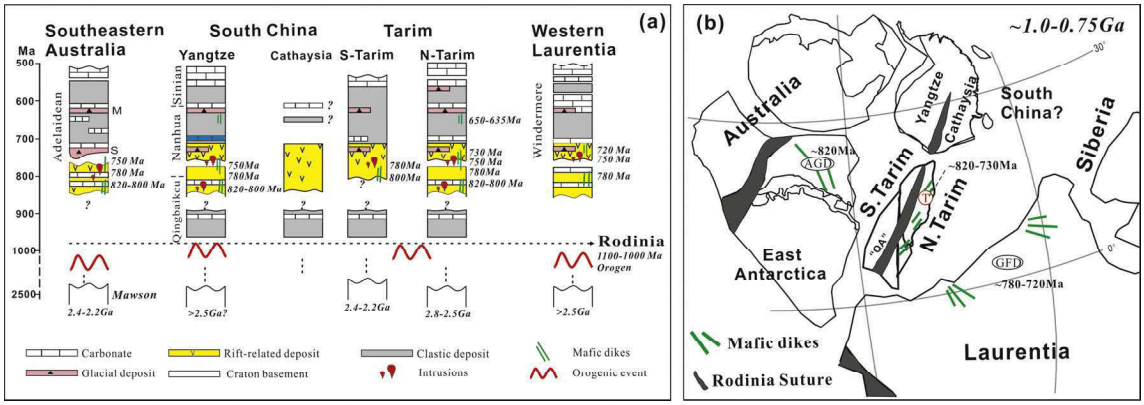

Fig. 9. (a) Tectonostratigraphic correlations between southeastern Australia, Tarim, South China and western Laurentia during the assembly and the rifting of Rodinia (modified after XBGMR, 1993; Li et al., 1995, 2008; Lu et al., 2008; Zhang et al., 2012; Z.Q. Xu et al., 2013; Wen et al., 2015). S/M, Sturtian/Marinoan glaciations. (b) Possible alternative/extended "missing-link" position for the Tarim Block in Rodinia, showing one optional position for South China, and schematic representations of Tonian mafic dike swarms (modified after Li et al., 1995, 2008; Lu et al., 2008; Zhang et al., 2012; Ernst et al., 2016). *AGD*, Amata–Gairdner Dyke Swarm (Sun and Sheraton, 1996; Wingate et al., 1998); *T*, mafic dikes or bimodal volcanic rocks in Tarim (Xu et al., 2005, 2009; Lu et al., 2008; Zhang et al., 2012); *GFD*, Gunbarrel–Franklin dike swarm (Harlan et al., 2003; Denyszyn et al., 2009). "QA", Quanji–Alxa block.

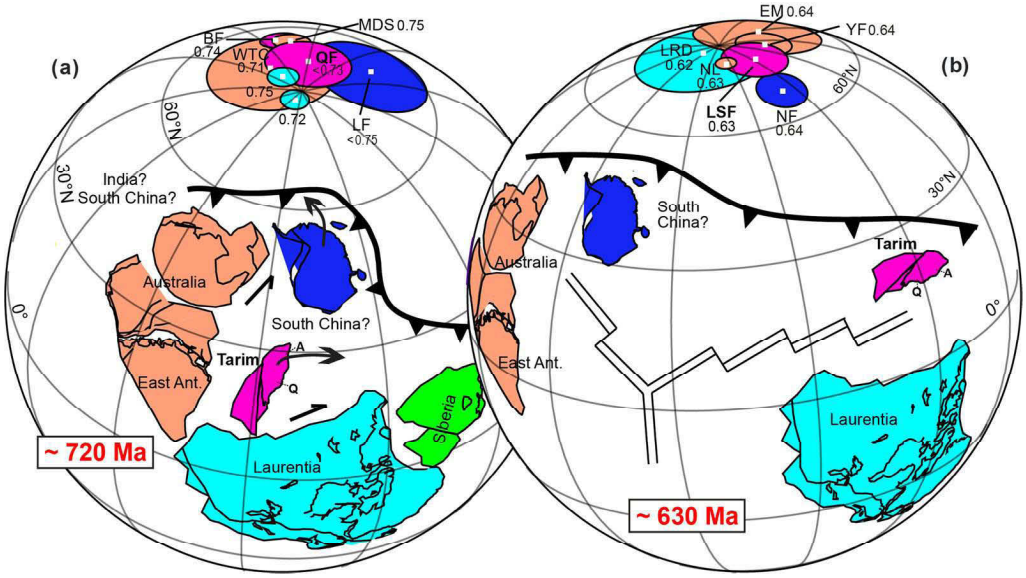

Fig. 10. Configuration and breakup of extended 'missing-link' model of Rodinia supercontinent. (a) 'Missing-link' position for the Tarim Block with the Baiyisi (BF; Huang et al., 2005) and Qiaoenbrak (QF; Wen et al., 2013) poles coincident with the coeval poles of other continents in the Rodinia model of Li and Evans (2011), showing the opposite rotation potential of Tarim and South China in the succeeding breakup process. Tarim Block is rotated relative to Laurentia using Euler rotation (86.3°N, 30.9°E, 135.7°). "A", Aksu–Wushi; "Q", Quruqtagh. Laurentia is reconstructed to the paleomagnetic reference frame using Euler rotation (47.7°N, 148.7°E, −198.6°). (b) One scene of reconstruction for the breakup of Rodinia following configuration shown in (a), showing the coincidence of ca. 625 Ma LSF pole from Tarim with those from other continents. Rotation of Laurentia (32.7°N, −157.6°E, −144.8°) to paleogeographic grid, Tarim (71.4°N, −20.0°E, 96.9°) relative to Laurentia, Australia–East Antarctica (31.0°N, −119.0°E, −68.0°), and South China (31.0°N, −119.0°E, −68.0°) relative to Australia–East Antarctica.

LF (Liantuo Fm) pole (Table 2). The ca. 720–630 Ma interval of breakup, determined herein paleomagnetically, is consistent with the age of rift–drift transition recognized in southeast Australia, South China and western Laurentia (Li and Evans, 2011, and references therein), as well as in Tarim where ca. 730–650 Ma bimodal magmatism related to rifting is recognized (e.g., Xu et al., 2005, 2009; Zhang et al., 2012). In this reconstruction, we discounted the poles from the Aksu dikes (Chen et al., 2004) and the Marinoan–Tereeken (ca. 635 Ma) cap carbonates from eastern Tianshan of NE Tarim (Zhao et al., 2014) for the following reasons. First, it should be noted that the oft-proposed connection between Tarim and northern Australia actually cannot be attained (Fig. 7b) by fitting the two cratons' apparent polar wander (APW) paths as claimed by Zhao et al. (2014); the figure in that paper is incorrectly rendered. Second, the Aksu dikes are constrained by a large range of ~800 to <720 Ma isotopic ages (Chen et al., 2004; Zhan et al., 2007; Zhu et al., 2011), and their exposures lie within the northern remagnetized area (sections *I* and *II*; Fig. 1a;) analyzed above; we suggest that the northern reaches of Aksu–Wushi area were affected by regional hydrothermal activity; both of the rejected poles are similar to the mid-Paleozoic Tarim apparent polar wander path (Fig. 7a), and the Tianshan belt indeed records Paleozoic (as well as Cenozoic) tectonism (e.g., Windley et al., 1990; Ge et al., 2012). We note further that a recent Sr isotope study (Wen et al., 2015) documented that the Marinoan–Tereeken cap carbonates in the Quruqtagh area (Fig. 1a) have experienced serious secondary alterations. The Baiyisi pole in Quruqtagh region seems curiously immune from the otherwise pervasive effects of remagnetization across that area.

In our model, by ca. 630 Ma, the extended missing-link Rodinia had broken apart (Fig. 10b), and the poles of Tarim and South China document significant antithetic rotations during this process (Fig. 10). The decrease in the ages of dike swarms from southeastern Australia, through Tarim, to western Laurentia (Fig. 9) indicates

Table 2
Paleomagnetic poles for the reconstructions shown in Fig. 10.

Block	Pole name	Rock unit (area)	Age (Ma)	Paleomagnetic pole		A_{95}	Reference
				Lat	Lon		
Tarim	LSF	Lower Sugetbrak Formation	620–630 Ma	−21.1	87.4	7.0	**This study**
	QF	Qiaoenbrak Formation	<730 Ma	−6.3	17.5	9.1	Wen et al. (2013)
	BF	Baiyisi Formation	750–730 Ma	−17.7	14.2	4.2	Huang et al. (2005)
Australia	WTC	Walsh Tillite cap dolomite	700–750 Ma	21.5	102.4	13.7	Li and Evans (2011)[a]
	MDS	Mundine Well Dykes	~750 Ma	45.3	135.4	4.1	Li and Evans (2011)[a]
	YF	Yaltipena Formation	~640 Ma	44.2	172.7	5.9	Li and Evans (2011)[a]
	EM	MEAN Elatina Formation	~635 Ma	49.9	164.4	13.5	Li and Evans (2011)[a]
	NL	Nuccaleena Fm	~630 Ma	32.3	170.8	2.2	Li and Evans (2011)[a]
Laurentia		Uinta Mountain Group	~750 Ma	0.8	161.3	3.3	Li and Evans (2011)[a]
		Franklin event grand mean	~720 Ma	6.7	162.1	3.0	Li and Evans (2011)[a]
	LRD	Long Range Dykes	~620 Ma	−19.0	175.3	14.8	Li and Evans (2011)[a]
South China	LF	Liantuo Formation	<750 Ma	4.4	161.1	12.9	Li and Evans (2011)[a]
	NF	Nantuo Formation	~640 Ma	0.2	151.2	5.4	Li and Evans (2011)[a]

Notes: Lat/Lon, latitude/longitude of a paleomagnetic pole. A_{95}, radius of the 95% confidence cone about the mean pole.
[a] The original references of the paleomagnetic poles can be found in the supplementary data file of Li and Evans (2011), which is available at http://www.geosociety.org/pubs/ft2011.htm, item 2011030.

propagation of rifting during Rodinia breakup. As the rifting proceeds, the larger blocks in Rodinia supercontinent (Australia and Laurentia) separate orthogonally and bear the record of plume-related magmatism; while smaller intervening blocks (Tarim including Quanji–Alxa, South China) experience large-scale vertical-axis rotations during separation (Fig. 10). Coincident with breakup and rotation, the present northern margin of Tarim experienced subduction-related magmatism (Ge et al., 2014). The coincidence in timing of supercontinental fragmentation with plume-related and subduction-related magmatism is reminiscent of the Mesozoic record of southern Gondwana breakup, which included both the ca. 183-Ma Karoo–Ferrar large igneous province (LIP) magmatism (Burgess et al., 2015) and subduction retreat along the Tasmanide orogen (Pankhurst et al., 2000). In that analogy, antithetic rotations of both the Falkland and Ellsworth–Whitmore Mountain blocks (Martin, 2007) are comparable to the complementary rotations of Tarim (clockwise) and perhaps South China (anticlockwise) during Rodinia breakup driven by back-arc rifting and slab rollback (Martin, 2006). If this conceptual model is correct, it can reconcile the apparent contradiction of mid-Neoproterozoic rifting and subduction in both South China and Tarim at about 800–700 Ma.

Alternatively, if South China is placed on the northwestern side of Australia (Jiang et al., 2003), then the Tarim "missing-link" model may require an additional, unknown, cratonic fragment to serve as the antithetic rotational entity. The various circum-Tarim terranes mentioned above may help to fill that role collectively, but with unknown initial geometry. Regardless of the exact configuration of central Asian terranes in a collective "missing link" location at the center of Rodinia, the model proposed herein hypothesizes upper-plate extension above a subduction zone as an important factor in supercontinental breakup. In the better-known example of Pangaea, initial stages of extension have recently been linked to subduction dynamics along the girdle of the supercontinent (Keppie, 2015). We suggest that subduction dynamics may play an important role in supercontinental breakup, for Pangea as well as Rodinia. Either the extended or the alternative 'missing-link' configuration supports a valid connection between Australia, Tarim, and Laurentia near the center of Rodinia at least until ~720 Ma. Rodinia supercontinent breakup, complementary to subduction rollback, retreat, and large-magnitude rotations of arc-bearing terranes in at least Tarim (if not other central Asian cratons), appears broadly similar to the Mesozoic breakup of southern Gondwana. Cratonic fragmentation assisted by marginal subduction-arc retreat may be an important phenomenon of global geodynamics through the supercontinent cycle.

Acknowledgements

We thank Shipeng Wang for field assistance, Huadong Ma for help with obtaining field permission, Joe Panzik for generous help at Yale, Mike Jackson, Dario Bilardello and Peter Solheid for analytical assistance at University of Minnesota, Joshua Feinberg for providing constructive suggestions, and Paul Hoffman and John Geissman for comments on an earlier version of the manuscript. Reconstructions were processed using software of GPlates (http://www.gplates.org). This research was supported by the National Natural Science Foundation of China (Nos. 41274071, 41230208) and Yale University. B. Wen is funded by a state scholarship grant from China Scholarship Council (CSC), a graduate research fellowship (No. 201501B027) from Nanjing University and a Visiting Research Fellowship from the Institute for Rock Magnetism, University of Minnesota. We would also like to thank Karl Karlstrom and two anonymous reviewers for their constructive comments that helped improve the paper greatly.

Appendix A. Supplementary material

Supplementary material related to this article can be found online at http://dx.doi.org/10.1016/j.epsl.2016.10.030.

References

Burgess, S.D., Bowring, S.A., Fleming, T.H., Elliot, D.H., 2015. High-precision geochronology links the Ferrar large igneous province with early-Jurassic ocean anoxia and biotic crisis. Earth Planet. Sci. Lett. 415, 90–99.
Calver, C.R., Crowley, J.L., Wingate, M.T.D., Evans, D.A.D., Raub, T.D., Schmitz, M.D., 2013. Globally synchronous Marinoan deglaciation indicated by U–Pb geochronology of the Cottons Breccia, Tasmania, Australia. Geology 41, 1127–1130.
Chen, Y., Xu, B., Zhan, S., Li, Y.A., 2004. First mid-Neoproterozoic paleomagnetic results from the Tarim Basin (NW China) and their geodynamic implications. Precambrian Res. 133, 271–281.
Cogné, J.P., 2003. PaleoMac: a Macintosh application for treating paleomagnetic data and making plate reconstructions. Geochem. Geophys. Geosyst. 4, 1–8.
Dalziel, I.W.D., 1997. Neoproterozoic–Paleozoic geography and tectonics: review, hypothesis, environmental speculation. Geol. Soc. Am. Bull. 109, 16–42.
Denyszyn, S.W., Halls, H.C., Davis, D.W., Evans, D.A.D., 2009. Paleomagnetism and U–Pb geochronology of Franklin dykes in High Arctic Canada and Greenland: a revised age and paleomagnetic pole constraining block rotations in the Nares Strait region. Can. J. Earth Sci. 46, 689–705.
Enkin, R.J., 2003. The direction-correction tilt test: an all-purpose tilt/fold test for paleomagnetic studies. Earth Planet. Sci. Lett. 212, 151–166.
Ernst, R.E., Hamilton, M.A., Soderlund, U., Hanes, J.A., Gladkochub, D.P., Okrugin, A.V., Kolotilina, T., Mekhonoshin, A.S., Bleeker, W., LeChminant, A.N., Buchan, K.L., Chamberlain, K.R., Didenko, A.N., 2016. Long-lived connection between southern Siberia and northern Laurentia in the Proterozoic. Nat. Geosci. 9, 464–470.

Evans, D.A.D., 2013. Reconstructing pre-Pangean supercontinents. Geol. Soc. Am. Bull. 125, 1735–1751.
Evans, D.A.D., Raub, T.D., 2011. Neoproterozoic glacial palaeolatitudes: a global update. Mem. Geol. Soc. Lond. 36, 93–112.
Fisher, R., 1953. Dispersion on a sphere. Proc. R. Soc. Lond. Ser. A 217, 295–305.
Foster, D.A., Mueller, P.A., Mogk, D.W., Wooden, J.L., Vogl, J.J., 2006. Proterozoic evolution of the western margin of the Wyoming craton: implications for the tectonic and magmatic evolution of the northern Rocky Mountains. Can. J. Earth Sci. 43, 1601–1619.
Gao, Z.J., Qian, J.X., 1985. Sinian glacial deposits in Xinjiang, northwestern China. Precambrian Res. 29, 143–147.
Gao, Z.J., Wang, W.Y., Peng, C.W., Li, Y.A., Xiao, B., 1985. The Sinian System of Xinjiang. Xinjiang People's Publishing House, Urumqi (in Chinese with English abstract).
Ge, R.F., Zhu, W.B., Wilde, S.A., He, J.W., Cui, X., Wang, X., Zheng, B.H., 2014. Neoproterozoic to Paleozoic long-lived accretionary orogeny in the northern Tarim Craton. Tectonics 33, 302–329.
Ge, R.F., Zhu, W.B., Wu, H.L., Zheng, B.H., Zhu, X.Q., He, J.W., 2012. The Paleozoic northern margin of the Tarim Craton: passive or active? Lithos 142–143, 1–15.
Glass, L.M., Phillips, D., 2006. The Kalkarindji continental flood basalt province: a new Cambrian large igneous province in Australia with possible links to faunal extinctions. Geology 34, 461–464.
Guo, Z.J., Yin, A., Robinson, A., Jia, C.Z., 2005. Geochronology and geochemistry of deep-drill-core samples from the basement of the central Tarim basin. J. Asian Earth Sci. 25, 45–56.
Halgedahl, S.L., Jarrard, R.D., 1995. Low-temperature behavior of single-domain through multidomain magnetite. Earth Planet. Sci. Lett. 130, 127–139.
Halverson, G.P., Hurtgen, M.T., Porter, S.M., Collins, A.S., 2010. Neoproterozoic–Cambrian biogeochemical evolution. Dev. Precambrian Geol. 16, 351–366.
Harlan, S.S., Heaman, L.M., LeCheminant, A.N., Premo, W.R., 2003. Gunbarrel mafic magmatic event: a key 780 Ma time marker for Rodinia plate reconstructions. Geology 31, 1053–1056.
He, J.W., Zhu, W.B., Ge, R.F., Zheng, B.H., Wu, H.L., 2014. Detrital zircon U–Pb ages and Hf isotopes of Neoproterozoic strata in the Aksu area, northwestern Tarim Craton: implications for supercontinent reconstruction and crustal evolution. Precambrian Res. 254, 194–209.
Hoffman, P.F., 1991. Did the breakout of Laurentia turn Gondwanaland inside-out? Science 252, 1409–1412.
Huang, B.C., Xu, B., Zhang, C.X., Li, Y.A., Zhu, R.X., 2005. Paleomagnetism of the Baiyisi volcanic rocks (ca. 740 Ma) of Tarim Northwest China: a continental fragment of Neoproterozoic Western Australia? Precambrian Res. 142, 83–92.
Jia, C.Z., Zhang, S.B., Wu, S.Z., 2004. Stratigraphy of the Tarim Basin and Adjacent Area. Science Publishing House, Beijing, pp. 1–450 (in Chinese with English abstract).
Jiang, G.Q., Sohl, L.E., Christie-Blick, N., 2003. Neoproterozoic stratigraphic comparison of the Lesser Himalaya (India) and Yangtze block (south China): paleogeographic implications. Geology 31, 917–920.
Jones, C.H., 2002. User-driven integrated software lives: "Paleomag" paleomagnetics analysis on the Macintosh. Comput. Geosci. 28, 1145–1151.
Karlstrom, K.E., Williams, M.L., McLelland, J., Geissman, J.W., Ahall, K.I., 1999. Refining Rodinia: geologic evidence for the Australia–Western U.S. connection in the Proterozoic. GSA Today 9, 1–7.
Keppie, D.F., 2015. How the closure of paleo-Tethys and Tethys oceans controlled the early breakup of Pangaea. Geology 43, 335–338.
Kirschvink, J.L., 1980. The least squares line and the analysis of paleomagnetic data. Geophys. J. R. Astron. Soc. 62, 699–718.
Kirschvink, J.L., 1992. Late Proterozoic low-latitude glaciation: the snowball Earth. In: Schopf, J.W., Klein, C. (Eds.), The Proterozoic Biosphere: A Multidisciplinary Study. Cambridge University Press, Cambridge, UK, pp. 51–52.
Kirschvink, J.L., Kopp, R.E., Raub, T.D., Baumgartner, C.T., Holt, J.W., 2008. Rapid, precise, and high-sensitivity acquisition of paleomagnetic and rock-magnetic data: development of a low-noise automatic sample changing system for superconducting rock magnetometers. Geochem. Geophys. Geosyst. 9, Q05Y01. http://dx.doi.org/10.1029/2007GC001856.
Knoll, A.H., Walter, M.R., Narbonne, G.M., Christie-Blick, N., 2006. The Ediacaran period: a new addition to the geologic time scale. Lethaia 39, 13–30.
Li, Y.P., McWilliams, M., Cox, A., Sharps, R., 1988. Late Permian paleomagnetic pole from dikes of the Tarim craton, China. Geology 16, 275–278.
Li, Z.X., Bogdanova, S.V., Collins, A.S., Davidson, A., De Waele, B., Ernst, R.E., Fitzsimons, I.C.W., Fuck, R.A., Gladkochub, D.P., Jacobs, J., Karlstrom, K.E., Lu, S., Natapov, L.M., Pease, V., Pisarevsky, S.A., Thrane, K., Vernikovsky, V., 2008. Assembly, configuration, and break-up history of Rodinia: a synthesis. Precambrian Res. 160, 179–210.
Li, Z.X., Evans, D.A.D., 2011. Late Neoproterozoic 40° intraplate rotation within Australia allows for a tighter-fitting and longer-lasting Rodinia. Geology 39, 39–42.
Li, Z.X., Evans, D.A.D., Halverson, G.P., 2013. Neoproterozoic glaciations in a revised global palaeogeography from the breakup of Rodinia to the assembly of Gondwanaland. Sediment. Geol. 294, 219–232.
Li, Z.X., Li, X.H., Kinny, P.D., Wang, J., Zhang, S., Hou, H., 2003. Geochronology of Neoproterozoic syn-rift magmatism in the Yangtze Craton, South China and correlations with other continents: evidence for a mantle superplume that broke up Rodinia. Precambrian Res. 122, 85–109.
Li, Z.X., Zhang, L., Powell, C.McA., 1996. Positions of the East Asian cratons in the Neoproterozoic supercontinen Rodinia. Aust. J. Earth Sci. 43, 593–604.
Li, Z.X., Zhang, L.H., Powell, C.McA., 1995. South China in Rodinia: part of the missing link between Australia–East Antarctica and Laurentia? Geology 23, 407–410.
Lowrie, W., 1990. Identification of ferromagnetic minerals in a rock by coercivity and unblocking temperature properties. Geophys. Res. Lett. 17, 159–162.
Lu, S.N., Li, H.K., Zhang, C.L., Niu, G.H., 2008. Geological and geochronological evidence for the Precambrian evolution of the Tarim Craton and surrounding continental fragments. Precambrian Res. 160, 94–107.
Ma, X.X., Shu, L.S., Santosh, M., Li, J.Y., 2012. Detrital zircon U–Pb geochronology and Hf isotope data from Central Tianshan suggesting a link with the Tarim Block: implications on Proterozoic supercontinent history. Precambrian Res. 206–207, 1–16.
Martin, A.K., 2006. Oppositely directed pairs of propagating rifts in back-arc basins: double saloon door seafloor spreading during subduction rollback. Tectonics 25, TC3008. http://dx.doi.org/10.1029/2005TC001885.
Martin, A.K., 2007. Gondwana breakup via double-saloon-door rifting and seafloor spreading in a backarc basin during subduction rollback. Tectonophysics 445, 245–272.
McElhinny, M.W., 1964. Statistical significance of the fold test in paleomagnetism. Geophys. J. R. Astron. Soc. 8, 33–40.
McFadden, P.L., McElhinny, M.W., 1990. Classification of the reversal test in paleomagnetism. Geophys. J. Int. 103, 725–729.
McMenamin, M.A.S., McMenamin, D.L.S., 1990. The Emergence of Animals: The Cambrian Breakthrough. Colombia University Press, New York. 217 pp.
Morin, F.J., 1950. Magnetic susceptibility of αFe_2O_3 and αFe_2O_3 with added Titanium. Phys. Rev. 78, 819–820.
Nakajima, T., Maruyama, S., Uchiumi, S., Liou, J.G., Wang, X., Xiao, X., Graham, S.A., 1990. Evidence for late Proterozoic subduction from 700-Myr-old blueschists in China. Nature 346, 262–265.
Pankhurst, R.J., Riley, T.R., Fannjing, C.M., Kelley, S.P., 2000. Episodic silicic volcanism in Patagonia and the Antarctic Peninsula: chronology of magmatism associated with the break-up of Gondwana. J. Petrol. 41, 605–625.
Payne, J.L., Hand, M., Barovich, K.M., Reid, A., Evans, D.A.D., 2009. Correlations and reconstruction models for the 2500–1500 Ma evolution of the Mawson Continent. In: Reddy, S.M., Mazumder, R., Evans, D.A.D., Collins, A.S. (Eds.), Palaeoproterozoic Supercontinents and Global Evolution. Geol. Soc. (Lond.) Spec. Publ. 323, 319–355.
Shu, L.S., Deng, X.L., Zhu, W.B., Ma, D.S., Xiao, W.J., 2011. Precambrian tectonic evolution of the Tarim Block, NW China: new geochronological insights from the Quruqtagh domain. J. Asian Earth Sci. 42, 774–790.
Song, S.G., Su, L., Li, X.H., Niu, Y.L., Zhang, L.F., 2012. Grenville-age orogenesis in the Qaidam–Qilian block: the link between South China and Tarim. Precambrian Res. 220–221, 9–22.
Sun, S.S., Sheraton, J.W., 1996. Geochemical and isotopic evolution. In: Glikson, A.Y., et al. (Eds.), Geology of the Western Musgrave Block, Central Australia, with Particular Reference to the Mafic–Ultramafic Giles Complex. Aust. Geol. Surv. Org. Bull. 239, 135–143.
Sun, W.H., Zhou, M.F., Yan, D.P., Li, J.W., Ma, Y.X., 2008. Provenance and tectonic setting of the Neoproterozoic Yanbian Group, western Yangtze Block (SW China). Precambrian Res. 167, 213–236.
Turner, S.A., 2010. Sedimentary record of Late Neoproterozoic rifting in the NW Tarim Basin, China. Precambrian Res. 181, 85–96.
Turner, S.A., Cosgrove, J.W., Liu, J.G., 2010. Controls on lateral structural variability along the Keping Shan Thrust Belt, SW Tien Shan Foreland, China. Geol. Soc. (Lond.) Spec. Publ. 348, 71–85.
Vervoort, J.D., Lewis, R.S., Fisher, C., Gaschnig, R.M., Jansen, A.C., Brewer, R., 2016. Neoarchean and Paleoproterozoic crystalline basement rocks of north-central Idaho: constraints on the formation of western Laurentia. Geol. Soc. Am. Bull. 128, 94–109.
Verwey, E.J., 1939. Electronic conduction of magnetite (Fe_3O_4) and its transition point at low temperature. Nature 144, 327–328.
Wang, C., Liu, L., Yang, W.Q., Zhu, X.H., Cao, Y.T., Kang, L., Chen, S.F., Li, R.S., He, S.P., 2013. Provenance and ages of the Altyn Complex in Altyn Tagh: implications for the early Neoproterozoic evolution of northwestern China. Precambrian Res. 230, 193–208.
Wang, X.L., Zhou, J.C., Griffin, W.L., Zhao, G.C., Yu, J.H., Qiu, J.S., Zhang, Y.J., Xing, G.F., 2014. Geochemical zonation across a Neoproterozoic orogenic belt: isotopic evidence from granitoids and metasedimentary rocks of the Jiangnan orogen, China. Precambrian Res. 242, 154–171.
Wen, B., Evans, D.A.D., Li, Y.X., Wang, Z.R., Liu, C., 2015. Newly discovered Neoproterozoic diamictite and cap carbonate (DCC) couplet in Tarim Craton, NW China: stratigraphy, geochemistry, and paleoenvironment. Precambrian Res., 278–294.
Wen, B., Li, Y.X., Zhu, W.B., 2013. Paleomagnetism of the Neoproterozoic diamictites of the Qiaoenbrak formation in the Aksu area, NW China: constraints on the paleogeographic position of the Tarim Block. Precambrian Res. 226, 75–90.
Windley, B.F., Allen, M.B., Zhang, C., Zhao, Z.Y., Wang, G.R., 1990. Paleozoic accretion and Cenozoic redeformation of the Chinese Tien Shan Range, central Asia. Geology 18, 128–131.

Wingate, M.T.D., Campbell, I.H., Compston, W., Gibson, G.M., 1998. Ion microprobe U–Pb ages for Neoproterozoic basaltic magmatism in south central Australia and implications for the breakup of Rodinia. Precambrian Res. 87, 135–159.

Wingate, M.T.D., Giddings, J.W., 2000. Age and palaeomagnetism of the Mundine Well dyke swarm, Western Australia: implications for an Australia–Laurentia connection at 755 Ma. Precambrian Res. 100, 335–357.

Wingate, M.T.D., Pisarevsky, S.A., Evans, D.A.D., 2002. Rodinia connections between Australia and Laurentia: no SWEAT, no AUSWUS? Terra Nova 14, 121–128.

Xinjiang Bureau of Geology and Mineralogy Resources (XBGMR), 1993. Regional Geology of Xinjiang Uygur Autonomy Region. Geology Publishing House, Beijing (in Chinese with English abstract).

Xu, B., Jian, P., Zheng, H.F., Zou, H.B., Zhang, L.F., Liu, D.Y., 2005. U–Pb zircon geochronology and geochemistry of Neoproterozoic volcanic rocks in the Tarim Block of northwest China: implications for the breakup of Rodinia supercontinent and Neoproterozoic glaciations. Precambrian Res. 136, 107–123.

Xu, B., Xiao, S.H., Zou, H.B., Chen, Y., Li, Z.X., Song, B., Liu, D.Y., Zhou, C.M., Yuan, X.L., 2009. SHRIMP zircon U–Pb age constraints on Neoproterozoic Quruqtagh diamictites in NW China. Precambrian Res. 168, 247–258.

Xu, B., Zou, H.B., Chen, Y., He, J.Y., Wang, Y., 2013. The Sugetbrak basalts from northwestern Tarim Block of northwest China: geochronology, geochemistry and implications for Rodinia breakup and ice age in the Late Neoproterozoic. Precambrian Res. 236, 214–226.

Xu, Z.Q., He, B.Z., Zhang, C.L., Zhang, J.X., Wang, Z.M., Cai, Z.H., 2013. Tectonic framework and crustal evolution of the Precambrian basement of the Tarim Block in NW China: new geochronological evidence from deep drilling samples. Precambrian Res. 235, 150–162.

Yao, J.X., Xiao, S.H., Yin, L.M., Li, G.X., Yuan, X.L., 2005. Basal Cambrian microfossils from the Yurtus and Xishanbulaq formations (Tarim, North-West China): systemic revision and biostratigraphic correlation of Micrhystridium-like acritarchs. Paleontology 48, 687–708.

Yue, Y.J., Ritts, B.D., Graham, S.A., 2001. Initiation and long-term slip history of the AltynTagh Fault. Int. Geol. Rev. 43, 1087–1093.

Zhan, S., Chen, Y., Xu, B., Wang, B., Faure, M., 2007. Late Neoproterozoic paleomagnetic results from the Sugetbrak Formation of the Aksu area, Tarim basin (NW China) and their implications to paleogeographic reconstructions and the snowball Earth hypothesis. Precambrian Res. 154, 143–158.

Zhang, C.L., Zou, H.B., Wang, H.Y., Li, H.K., Ye, H.M., 2012. Multiple phases of the Neoproterozoic igneous activity in Quruqtagh of the northeastern Tarim Block, NW China: interaction between plate subduction and mantle plume? Precambrian Res. 222–223, 488–502.

Zhang, S.H., Evans, D.A.D., Li, H.Y., Wu, H.C., Jiang, G.Q., Dong, J., Zhao, Q.L., Raub, T.D., Yang, T.S., 2013. Paleomagnetism of the late Cryogenian Nantuo Formation and paleogeographic implications for the South China Block. J. Asian Earth Sci. 72, 164–177.

Zhao, J.H., Zhou, M.F., Yan, D.P., Zheng, J.P., Li, J.W., 2011. Reappraisal of the ages of Neoproterozoic strata in South China: no connection with the Grenvillian orogeny. Geology 39, 299–302.

Zhao, P., Chen, Y., Zhan, S., Xu, B., Faure, M., 2014. The apparent polar wander path of the Tarim block (NW China) since the Neoproterozoic and its implications for a long-term Tarim–Australia connection. Precambrian Res. 242, 39–57.

Zhu, M.Y., Wang, H.F., 2011. Neoproterozoic glaciogenic diamictites of the Tarim Block, NW China. Mem. Geol. Soc. Lond. 36, 367–378.

Zhu, W.B., Zheng, B.H., Shu, L.S., Ma, D.S., Wu, H.L., Li, Y.X., Huang, W.T., Yu, J.J., 2011. Neoproterozoic tectonic evolution of the Precambrian Aksu blueschist terrane, northwestern Tarim, China: insights from LA-ICP-MS zircon U–Pb ages and geochemical data. Precambrian Res. 185, 215–230.